ISSN: 1847-9286
Open Access Journal
www.jese-online.org

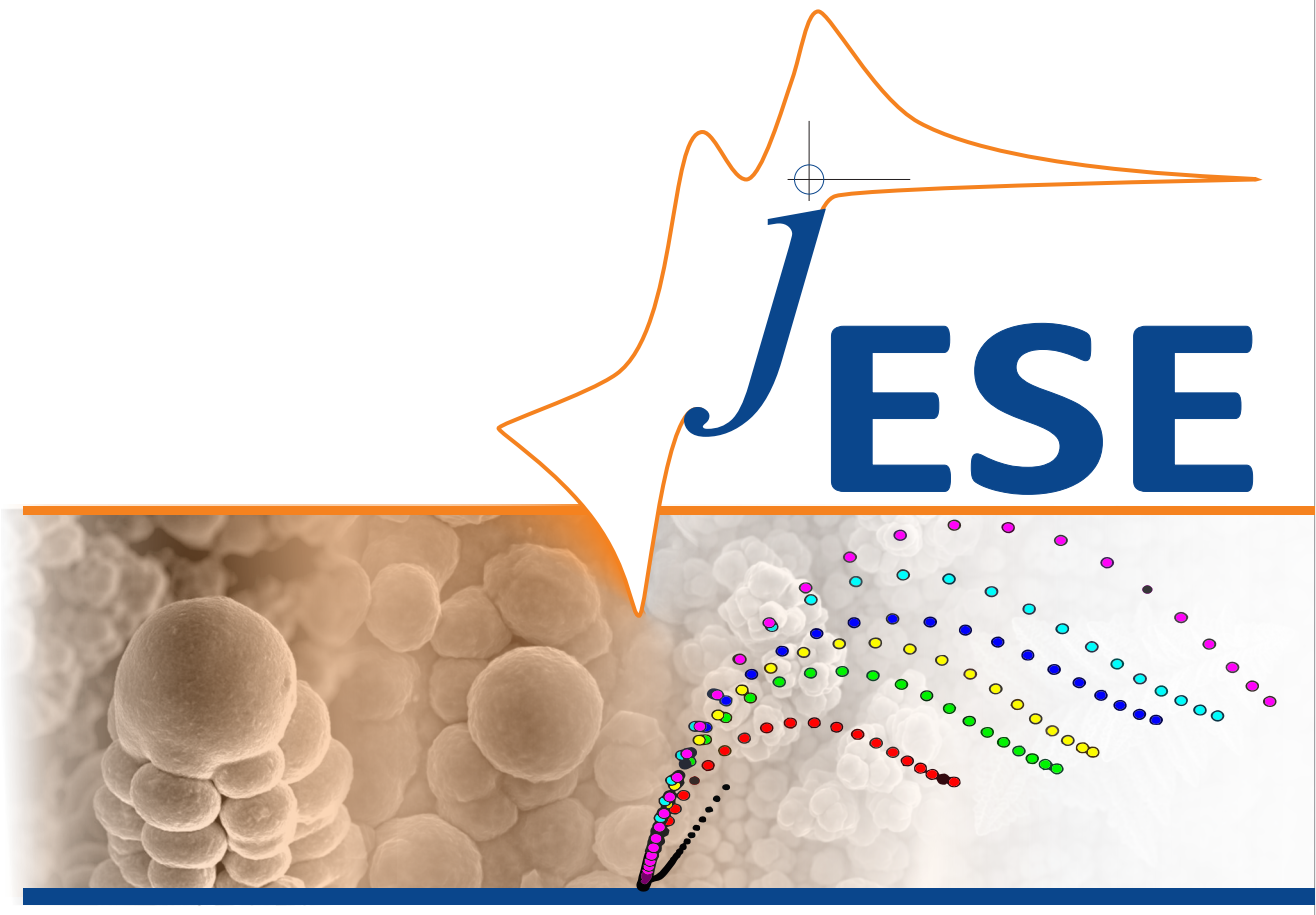

Journal of Electrochemical Science and Engineering

J. Electrochem. Sci. Eng. **6**(**2**) 2016, 155-213

IAPC Publishing

J. Electrochem. Sci. Eng. **6(2)** (2016) 155-164; doi: **10.5599/jese.205**

Open Access : : ISSN 1847-9286

www.jESE-online.org

Original scientific paper

Spectroscopic, voltammetry and molecular docking study of binding interaction of antipsychotic drug with bovine serum albumin

Mallappa Mahanthappa, Babu Giriya Gowda✉, Jayant I. Gowda*, Raghavendran Rengaswamy

Department of Chemistry, Maharani's Science College for Women, Bangalore-560 001, India
**P.G. Department of Studies in Chemistry, Karnatak University, Dharwad- 580 003, India*

✉Corresponding Author: babgowda@gmail.com, Phone: +91-9900475412

Received: July 22, 2015; Accepted: February 4, 2016

Abstract

The interaction between perazine dimaleate (PDM) and bovine serum albumin (BSA) was investigated by voltammetry, fluorescence spectroscopy, UV–vis spectroscopy, molecular docking and viscometric methods. The study was carried out in acetate buffer solution of pH 7.2, which was prepared by using 0.1 M sodium acetate and adjusting pH using 0.1 M hydrochloric acid. The voltammetric study of PDM shows a pair of well redox peaks at 0.538 and 0.471 V (versus SCE) on a GCE in acetate buffer of pH 7.2 at 50 mV s^{-1}. After the addition of BSA into the PDM solution, the redox peak currents decreased gradually, and peak potentials shifted towards negative direction. The results of voltammetry, fluorescence quenching and UV–vis absorption spectra experiments indicated the formation BSA–PDM complex. The binding parameters like binding constant and binding free energy were determined from voltammetric data. The binding constant and binding energy was also determined from UV–vis and fluorescence spectroscopy with a value quite close to that obtained from CV.

Keywords

Bovine serum albumin; Perazine dimaleate; Cyclic Voltammetry; Spectroscopy; Molecular docking; Binding Constant; Binding energy

Introduction

The drug–protein interaction is a fundamental issue in life process that helps us to understand the absorption, transport, metabolism and the target molecules of the drugs at the cellular level

[1-3]. Serum albumins are the major soluble protein constituents of the circulatory system possessing many physiological functions of which the most important are serving as a depot and a transport protein for many endogenous and exogenous compounds such as drugs [4]. The interaction of drugs with serum albumin is great aspect and various types of application in research field in chemistry, life science and clinical medicine [5-8]. Bovine serum albumin (BSA) has been widely investigated due to its structural homology with human serum albumin [9]. Intercalation, groove binding, and electrostatic interactions are the three major binding modes of small molecules to BSA [10].

Perazine dimaleate (PDM) is biologically active drug, chemically known as 10-[3-(4 methylpiperazine-1-yl)propyl]-10-phenothiazine·2maleicacid; perazine maleate; Pernazinum (Fig. 1). PDM is important class of tricyclic compounds belongs to the phenothiazine family drugs. Generally, phenothiazine drugs are widely used as antiemetic, sedative and analgesic because they are able to reduce the side effects of chemotherapy and they they also have a role in inhibiting tumor cell proliferation. These drugs can also reduce anxiety, insomnia and other symptoms related to the psychological state of cancer patients [11].

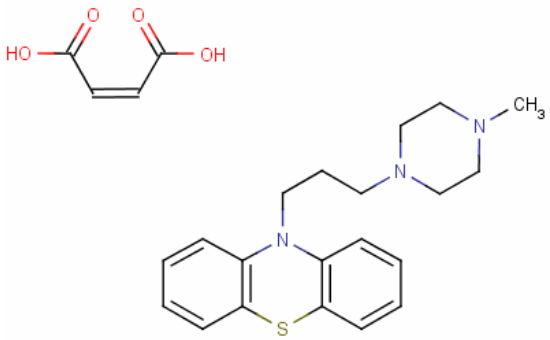

Fig. 1. *Chemical structure of perazine dimaleate (PDM)*

There has not any report about the study of PDM–BSA interaction based on the voltammetry behaviours at GCE and more than ever on the change of spectroscopic characteristics. Accordingly, in this work, investigations of the voltammetric behaviour of PDM upon addition of BSA were carried out. Moreover, the changes in the UV-Vis absorption and fluorescence emission when PDM binding to BSA were used to study the mode of such interaction. The results of voltammetry and spectroscopic techniques confirmed each other. The interaction study of PDM with BSA gives the information about the quenching mechanisms, binding constant, binding mode and number of binding sites. The advantage of this method is simple, rapid, accurate and inexpensive.

Materials and methods

PDM sample was donated by Global Calcium Ltd., Hosur. Stock solution, 1.0 mmol L^{-1} of PDM was prepared by dissolving an appropriate amount of the drug in doubly distilled water. BSA (Sigma–Aldrich) was used without further purification and its stock solution was prepared by dissolving an appropriate amount of BSA in doubly distilled water and stored at 4 °C. The concentration of BSA in stock solution was determined by UV absorption at 260 nm using a molar absorption coefficient ε_{260} = 66,000 L mol^{-1} cm^{-1}. Purity of the BSA was checked by monitoring the ratio of the absorbance at 260 nm to that at 280 nm [12]. The supporting electrolyte used for 0.1 M acetate buffer solution of pH 7.2, which was prepared by using 0.1 M sodium acetate and pH was adjusted by using 0.1M acetic acid and all the experiments were conducted in this buffer

at 25 °C. All other reagents used were of analytical grade and doubly distilled water was used throughout the experiment.

Instrumentation

Voltammetric measurements were performed using a CH electrochemical analyzer. A conventional three-electrode cell was employed throughout the experiments, with glassy carbon electrode (3.0 mm diameter) as a working electrode, a saturated calomel electrode (SCE) as a reference electrode, and a platinum electrode as a counter electrode.

Absorption spectra were measured on Ellico UV-visible spectrophotometer. The electronic spectrum of a known concentration of the drug was obtained without BSA. The spectroscopic response of the same amount of the drug was then monitored by the addition of small aliquots of BSA solution. All of the samples were mixed properly and allowed to equilibrate for 5 min prior to every spectroscopic measurement.

The viscosity measurements were carried out using Ostwald viscometer. The pH measurements were made with Scott Gerate pH meter CG 804. An electronic thermostat water-bath was used for controlling the temperature.

The steady-state fluorescence spectra were recorded using an F-2700 spectrofluorometer (Japan). The fluorescence emission spectrum of PDM (excitation at 250 nm) was used to obtain the intensities of the peaks. Good resolution of the bands was obtained at the slit width (ex. 10.0 nm; em.10.0 nm). The scan range used was from 300 to 600 nm.

The molecular docking studies of BSA with compounds were achieved by using Auto dock Vina, developed at the Scripps research institute (http://vina.scripps.edu) [13]. The input files for AutoDock Vina were prepared with AutoDock Tools (ADT), which is a Graphical User Interface for AutoDock and AutoDock Vina. The crystal structure of bovine serum albumin (3V03) was retrieved from Protein data bank and the ligand binding site location was analyzed by Q-Site Finder [14]. The co-crystallized ligand was removed. Using ADT the water molecules were removed from the protein and polar hydrogen were added followed by adding Kollman charges. The Grid box has been set according to the binding site on protein and saved as pdbqt format, which was required by AutoDock Vina. The 2 dimensional structure of ligand were drawn by Chem sketch and converted to PDB format, required by AutoDock Tools by Open Babel [15]. The rotatable bonds were selected within the ligand using Choose Torsions option in ADT and saved in pdbqt format The Lamarckian Genetic Algorithm (LGA), which is a novel and robust automated docking method available in AutoDock [16], was employed.

Results and discussion

Voltammetric studies of interaction of PDM with BSA

The Voltammetric behaviour of 1.5 x 10^{-4} M PDM in the absence and presence of BSA on bare GCE at 50mV s^{-1} is shown in Fig. 2. The voltammogram without BSA featured a couple of well defined and stable redox peaks in the potential range of 0.0 – 1.0 V. The anodic and cathodic peaks were appeared at 0.538 and 0.471 V *vs.* SCE with a formal potential (E^0) of 0.5045 V. The formal potential (E^o) in all voltammetric studies, predictable as the midpoint of reduction and oxidation potentials. By the addition of 5 - 30 µmol L^{-1} of BSA into 1.5×10^{-4} M drug (Fig. 2) the anodic peak potential was shifted towards negative direction and also peak current was decreased. The substantial decrease in peak current indicates the formation of PDM–BSA complex.

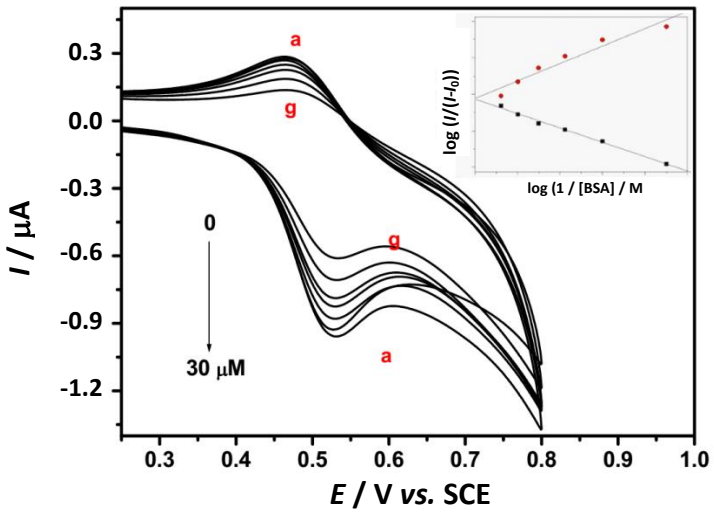

Fig. 2. *Cyclic voltammogram of 1.5 x 10^{-4} M PDM in the absence of BSA and in presence of C_{BSA} = 0, 5, 10, 15, 20, 25, 30 µmol L^{-1} (a to g) BSA in acetate buffer of pH-7.2 at 50 mV s^{-1} and inset of the plot of log (1/[BSA])* vs. *log (I/ (I_0 −I)).*

The mode of PDM–BSA interaction can be well-known from the variation in formal potential. In general the positive shift (anodic shift) in formal potential is caused by the intercalation of the drug with BSA [17], while negative shift is observed for the electrostatic interaction of the drug with BSA [18]. Therefore, this is evident that negative peak potential shift (cathodic shift) in the CV behaviour of PDM by the addition of BSA is attributable to the electrostatic interaction of PDM with BSA. The cathodic peak potential shift further indicates that PDM is easier to oxidize in presence of BSA because its oxidized form is more strongly bound to BSA than its reduced form. In this system, both forms of the drug interact with BSA.

Based upon the decrease in peak current of PDM by the various concentration of BSA, the binding constant was calculated according to the following equation [19]:

$$\log (1/[BSA]) = \log K + \log (I/I_0\text{-}I)$$

where, K is the binding constant, I_0 and I are the peak currents of the free PDM and PDM–BSA complex, respectively. The plot of log (1/[BSA]) *vs.* log (I/(I_0 −I)) constructed (inset of Fig. 2). From the linear fitting, the binding constant (K) can be estimated from the intercept. With this procedure, we obtained K = 4.591×10^4 L M^{-1} and the correlation coefficient was found as 0.99649.

Influence of scan rate

The voltammetric behavior of 1.5×10^{-4} M PDM in the absence and presence of BSA at bare GCE is shown in Fig. 3. The CVs of the 1.5×10^{-4} M PDM on GCE in 0.1 M acetate buffer solution at pH 7.2 shows pair of well defined and stable redox peaks in the potential range of 0.0 – 1.0 V. An increase in the scan rate, peak potential does not shift but peak currents of both anodic as well as cathodic increased linearly. The scan rate varies from 10 to 400 mV s^{-1}. At the same time, the cathodic and anodic peak currents increased linearly with the scan rate (Fig. 3) and the redox peak currents increased linearly with the scan rate, the correlation coefficient was 0.9919 for cathodic peak and 0.9944 for anodic peak respectively. The redox process is diffusion-controlled as shown by I_{peak} versus $\upsilon^{1/2}$ plot inset of Fig. 3. This was further confirmed by the plot of log I_{peak} *vs.* log υ, which was linear within the same scan rate range and gave a slope of 0.5606 [Figure as not shown]. This value is very close to the theoretical value of 0.5 reported by Laviron for a diffusion-controlled

electrode process [20]. This phenomenon suggested that the redox process was a diffusion controlled and the PDM was stable.

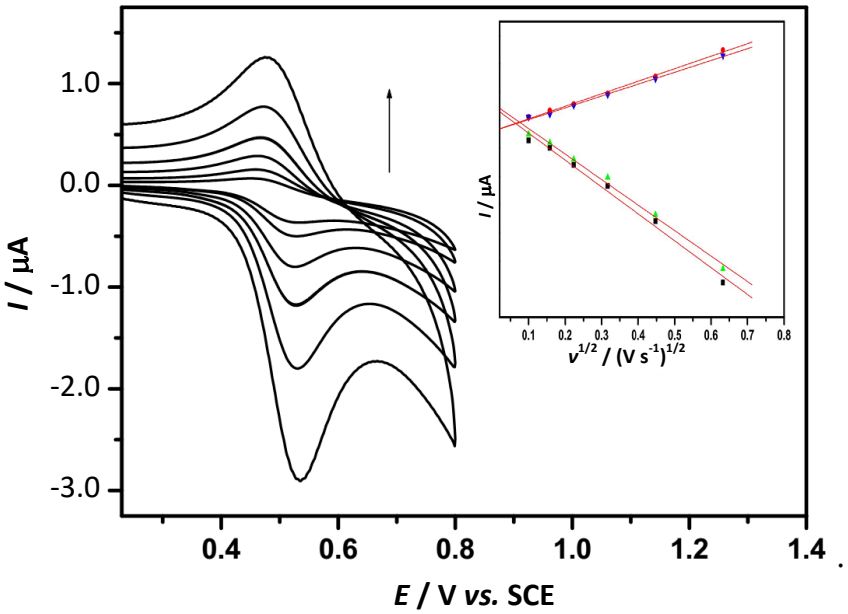

Fig. 3 *Cyclic voltammograms of 1.5 x 10^{-4} M PDM at various scan rates: 10, 25, 50, 100, 200, 400 mV s^{-1} respectively. Inset, plot of I_{peak} versus $\upsilon^{1/2}$ (Red and black points are before addition of BSA and blue and green points are after addition of BSA)*

The redox peak of PDM is attributed to the one electron which involved reduction and oxidation of PDM to PDM free radical [21].

$$PDM \underset{e^-}{\overset{-e^-}{\rightleftharpoons}} [PDM]^{\bullet +}$$

The electron transfer rate constant (k_s) is calculated using Laviron's equations [21-23] as follows:

$$E = E^0 - 2.3RT \log (v/\alpha nF)$$

$$E = E^0 - 2.3RT \log (v/(1-\alpha)nF)$$

$$\log k_s = \log(1-\alpha) + (1-\alpha) \log \alpha - \log (RT/nFv) - \alpha(1-\alpha)nF\Delta E_p/2.303RT$$

Where α is the electron transfer coefficient, n is the number of electrons transferred (n = 1). R = 8.314 J mol^{-1} K^{-1}, T = 298 K and F = 96493 C/mol are gas, temperature and Faraday constant, respectively and k_s is the electron transfer rate constant which can be calculated according to the plot of ΔE_p versus ln v. It is found to be 0.9890 s^{-1} in absence of BSA and 1.101 s^{-1} in presence of BSA. From the results of the above experiments, the formation of an electrochemically non-active complex of PDM with BSA resulted in the decrease of the free concentration of PDM in the reaction solution which caused the decrease of the peak currents. There is no appreciable difference in the value of k_0 in presence and absence of BSA indicating that BSA did not alter the voltammetric kinetics of PDM.

Absorption spectral behaviour of PDM with BSA

The UV-visible absorption titration is simple and more effective method for getting further clues about the mode of interaction and binding strength. Figure. 4 show the electronic absorption spectra of 1.5×10^{-4} M PDM in the absence and presence of different concentrations of BSA. The

absorbance of PDM was located around at 248 nm. The maximum absorption of the drug at this wavelength exhibited slight bathochromic shift and pronounce hyperchromic shifts by the incremental addition of BSA. The bathochromic shift is associated with the decrease in energy gap between the highest (HOMO) and lowest (LUMO) molecular orbitals after interaction of PDM to BSA [24]. The compactness in the structure of either the drug alone and/or BSA after the formation of drug-BSA complex may result in hyperchromism. Meanwhile, PDM molecule is inserted into the cavities of BSA and disrupted the original structures of BSA. This results which confirms the crystal structure of BSA had changed and there was a strong interaction between PDM and BSA.

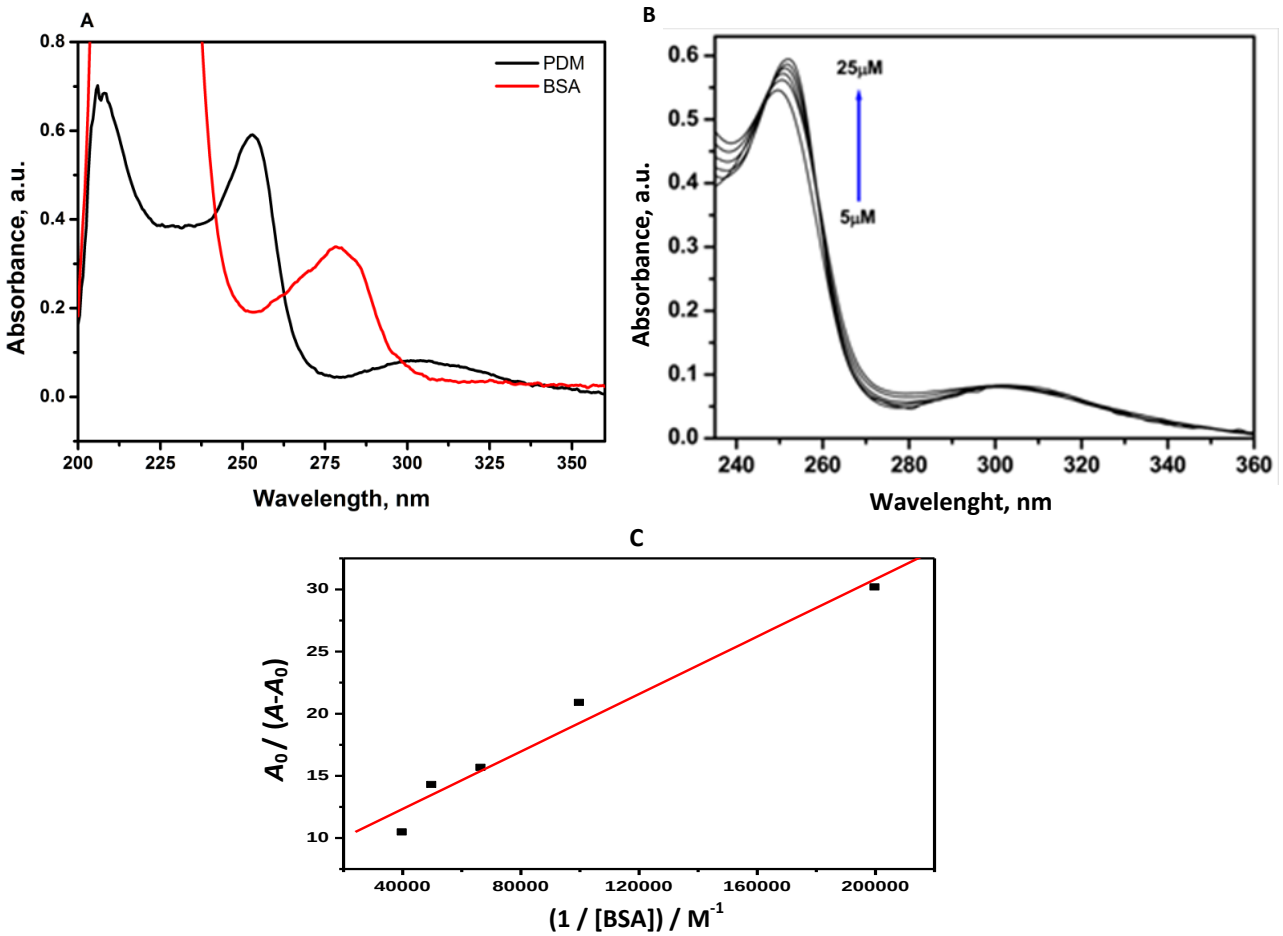

Figure. 4 *UV-visible spectra of* ***(A)*** *PDM and BSA,* ***(B)*** *1.5 x 10^{-4} M PDM in the absence of BSA and the presence of* [BSA] = *5.0, 10.0, 15.0, 20.0, 25.0 and 30.0 µmol BSA in acetate buffer of pH 7.2.* ***(C)*** *The plot of* (A_0 / (A-A_0)) *versus 1 / [BSA].*

Based upon the increase in absorbance, the binding constant (K_b) was calculated according to the following equation [24].

$$A_0/(A-A_0) = \varepsilon_G/(\varepsilon_{H\text{-}G} - \varepsilon_G) + \varepsilon_G/(\varepsilon_{H\text{-}G} - \varepsilon_G) \times 1/K[BSA]$$

Where, A_0 and A are the absorbance of PDM in the absence and presence of BSA, ε_G and ε_{H-G} are the absorption coefficients of PDM and its complex with BSA, respectively.

The slope to intercept ratio of the plot between $A_0/(A- A_0)$ *vs.* 1 / [BSA] yielded the binding constant, $K = 6.6671\times10^4$ L M^{-1}, which is close to the value of $K = 1.9824\times10^4$ L M^{-1} obtained from CV. The moderate binding constant indicative of electrostatic interaction and the Gibbs energy

change ($\Delta G = -RT \ln K$) of approximately 24.039 kJ mol^{-1} at 25 °C signifies the spontaneity of interaction of PDM with BSA.

The type of quenching mechanism was determined using UV-visible absorption spectroscopy. Quenching usually occurs either by static or dynamic mode. Static quenching refers to fluorophore–quencher complex formation and the dynamic quenching refers to a process that the fluorophore and the quencher come into contact during the transient existence of the excited state. However, the formation of non-fluorescence ground-state complex induced the change in absorption spectrum of fluorophore. Addition of the BSA to PDM leads to an increase in PDM absorption intensity without affecting the position of absorption band (Fig. 4A). It showed the existence of static interaction between BSA and the complexes.

Spectrofluorimetric spectral behaviour of PDM-BSA complex

The interaction of PDM with BSA was also examined by fluorescence titration. The fluorescence emission spectra of BSA in the presence and absence of various concentration of PDM is shown in Fig. 5. The maximum emission of BSA is located at 342 nm (λ_{ex} = 263 nm). The fluorescence emission maxima were gradually decreased with increase in concentration of PDM, indicating the quenching of fluorescence intensity of BSA upon binding to PDM. This can be attributed to the formation of PDM-BSA complex. The results suggest that microenvironment around the chromospheres of BSA is changed and it shows the strong interaction between PDM and BSA [25].

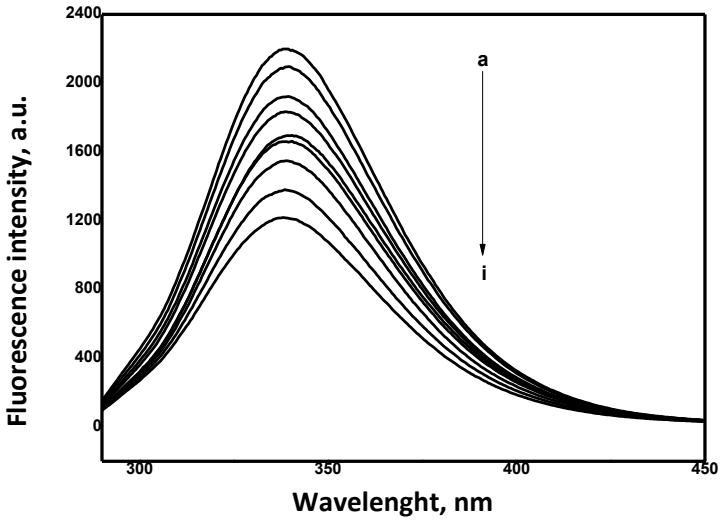

Fig. 5. *Fluorescence spectra of 1.5×10^{-4} M BSA in presence of* C_{PDM} *= 0, 5, 10, 15, 20, 25, 30, 35 µmol L^{-1}.*

Stern-Volmer binding and quenching constant

To determine the quenching mechanism between BSA and PDM (*i.e.* dynamic or static quenching), the fluorescence quenching data were analyzed using Stern-Volmer equation.

$$F_0 / F = 1 + k_q \tau_o [Q] = 1 + K_{sv} [Q]$$

where, F_0 and F are the fluorescence intensities of BSA in absence and presence of PDM respectively, [Q] is the Concentration of BSA and k_q is the quenching rate constant of the biomolecule, τ_o is the average excited-state life time and K_{sv} is the Stern-Volmer quenching constant.

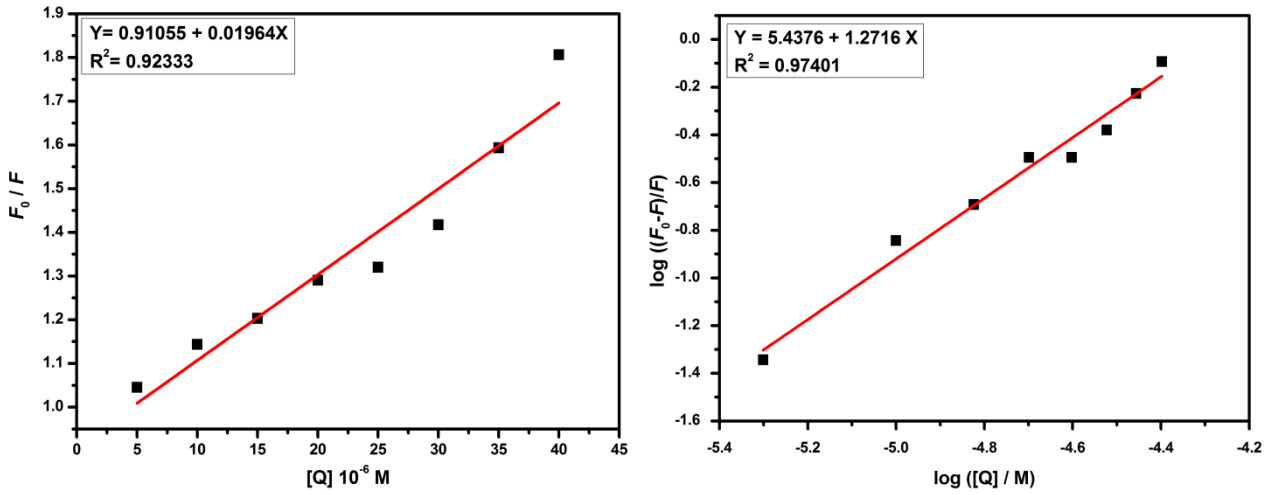

Fig. 6 (a) *Plot of* F_0/F versus *[Q] and* ***(b)*** *Plot of log [*$(F_0-F)/F$*]* versus *log [Q]*

The K_{sv} is stern-volmer quenching constant, which was determined by linear regression of a plot of F_0/F *vs.* [Q] at 25 °C was constructed (Fig. 6a) using the data from fluorescence titration and a linear fitting of the data yielded the binding constant 2.4158×10^4 L M^{-1} which is good agreement with result obtained from CV and UV/vis spectroscopy. The maximum rate constant of collisional quenching of various quenchers with biopolymers is about 2.0 x 10^{10} L s^{-1} mol^{-1} [25]. The greater value for K_q is obtained (K_{sv} and k_q values calculated were 1.964×10^4 L M^{-1} and 1.964×10^{12} L M^{-1} s^{-1}) (R^2 = 0.99523) respectively. As temperature increased, the decreasing trend of K_q was in accordance with K_{sv}'s dependency on temperature, which coincided with a static quenching mechanism. The binding of PDM to BSA was reduced as temperature increased, which suggests that the fluorescence quenching process may be mainly controlled by static quenching mechanism rather than dynamic.

The binding constant and number of binding sites

The binding constant and number of binding sites for PDM-BSA were determined by the following equation [26]:

$$\log[(F_0-F)/F] = \log K_b + n \log [Q]$$

where, K_b is binding constant and n is number of binding sites in base pair units respectively. The values of n and K_b can be determined from the slope and intercept of the double logarithm regression curve log [(log [$(F_0 - F)/F$] *vs.* log [Q]) (Fig. 6b). The binding constant value 5.43×104 L M^{-1} (R^2 = 0.99879) and values of n is found to be 1.2 ≈ 1.0, indicating that there is one independent class of binding sites in BSA for PDM. The free energy change, ΔG^0 (at 27 °C) was evaluated from K_b using the relationship $\Delta G^0 = -2.303RT \log K_b$ and its value was found to be -27.016 kJ M^{-1} indicating the spontaneity of the reaction.

Molecular modeling studies

Molecular docking was performed to study the interaction between PDM and BSA to determine the preferred binding site and binding mode. The best confirmation was determined based on binding affinity and RMSD. The binding energy and RMSD was performed by Auto Dock Vina. A three dimensional docked structure of PDM on BSA was shown in Fig. 7. These structures were to study various inter molecular interaction and to determine the binding energy of the docked

complexes. The PDM were docked with receptor BSA using the parameters mentioned above. The energy of interaction for PDM-BSA complex was found to be -10.0 kcal mol^{-1}.

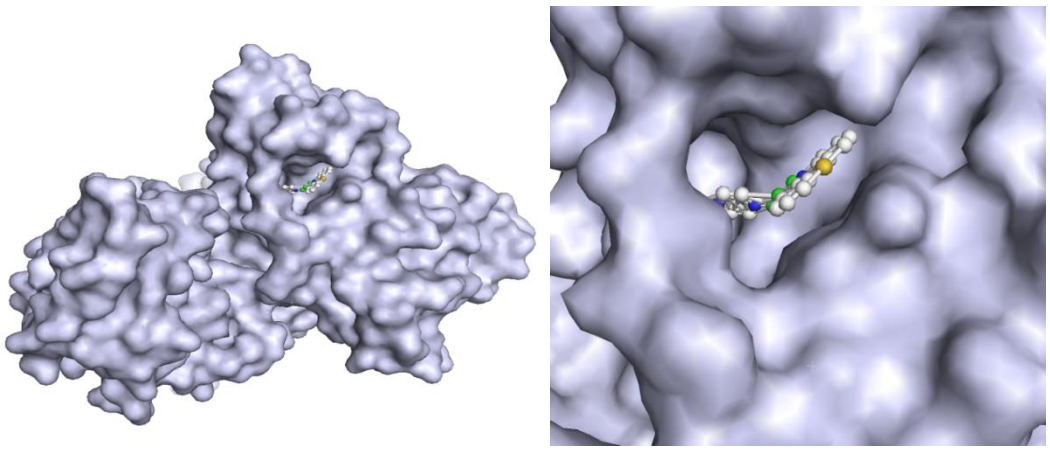

Fig. 7. *Molecular model of the surface and the active site of the complex of PDM (stick) and BSA (white surface)*

Viscometer measurement

Viscometric technique is an effective tool in clarifying the mode of interaction of small molecules with BSA under the physiological condition. In general, intercalation (in-binding mode) causes an increase viscosity of BSA solution due to lengthening the BSA widened to accommodate the bonded molecule [27]. The reverse can be taken for the electrostatic interaction. The value of relative specific viscosity $(\eta/\eta_0)^{1/3}$ *vs.* [BSA]/[PDM] were plotted (Fig. 8). However, the relative viscosity of BSA dependence upon the concentration of PDM, the value of [BSA]/[PDM] is decreased. This behaviour indicates that the binding mode between BSA and PDM should be non-classical intercalation or groove mode via hydrophobic interaction.

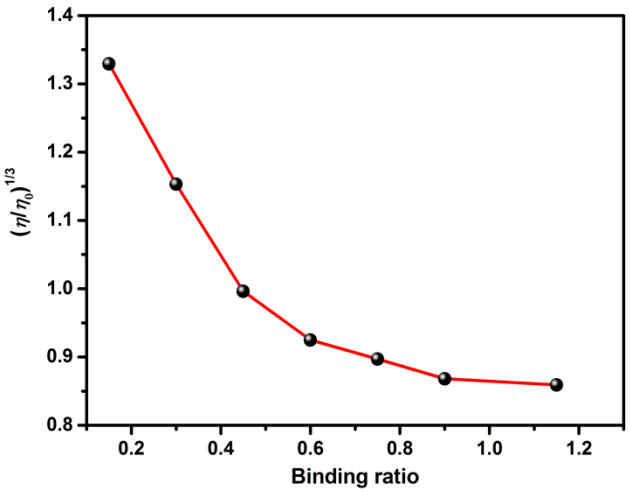

Fig. 8. *Plot of [BSA/PDM]* ***vs.*** *$(\eta/\eta_0)^{1/3}$*

Conclusions

In this work, the interaction of PDM with BSA was studied by voltammetric, spectroscopic and viscometric methods. In voltammetric studies, it was observed that the presence of BSA in a solution of perazine dimalaete reduces the equilibrium concentration of free perazine dimalaete and produces a voltammetric inactive complex. Both electrostatic interactions and minor groove binding modes were deduced from the results of different methods applied to the system,

although groove binding seemed to be predominant. Meanwhile, the experimental results indicate that the quenching mechanism of fluorescence of BSA by PDM is a static quenching procedure and the binding reaction is spontaneous. This work provides some significant information to clinical research about PDM and the theoretical basis for new drug designing.

Acknowledgement: *The authors are grateful for the financial support provided by the University Grants Commission, New Delhi, India (F. No. 42-308/2013 (SR) Dated 28/03/2013). Thanks are also due to Global Calcium Ltd., Hosur for supplying gift samples of PDM. Thanks are also due to Dr. Siddalingeshwar, Department of Physics, MSRIT, Bangalore for providing spectrofluorimetric instrumental facility*

References

[1] E. La Zaro, P. J. Lowe, X. Briand, B. Faller, *J. Med. Chem.* **51** (2008) 2009-2017.
[2] B. Ahmad, S. Parveen, R.H. Khan, *Bio-macromolecules* **7** (2006) 1350-1356.
[3] F. Bosca, *J. Phys. Chem. B* **116** (2012) 3504-3511.
[4] R. E. Olson, D.D. Christ, *Ann. Rep. Med. Chem.* **31** (1996) 327-336.
[5] E. Ahmad, G. Rabbani, N. Zaidi, S. Singh, M. Rehan, M. M. Khan, S. K. Rahman, Z. Qadri, M. Shadab, M. T Ashraf, N. Subbarao, R. Bhat, R. H. Khan, *PLoS One* **6(11)** (2011) e26186 1-18.
[6] E. Ahmad, P. Sen, R.H. Khan, *Cell. Biochem. Biophys.* **61** (2011) 313-325.
[7] G. K Wang, X. Li, X. L. Ding, D. C. Wang, C. L Yan, Y. Lu, *J. Pharm. Biomed. Anal.* **55** (2011) 1223-1226.
[8] F. P Nicoletti, B. D. Howes, M. Fittipaldi, G. Fanali, M. Fasano, P. Ascenzi, G Smulevich, *J. Am. Chem. Soc.* **130** (2008) 11677–11688.
[9] F. Thomas, P. Rochaix, M. White-Koning, I. Hennebelle, J. Sarini, A. Benlyazid, L. Malard, J. Lefebvre, E. Chatelut, J. P. Delord, *Eur. J. Cancer*. **45** (2009) 2316- 2323.
[10] B. M. Zeglis, V. C. Pierre, J. K. Barton, *Chem. Commun*. **44** (2007) 4565–4579.
[11] Q. Lu, D.Y. Qing, *Sci. China. Life Sci.* **56** (2013) 1020-1027.
[12] M. E. Reichmann, S. A. Rice, C. A. Thomas, P. Doty, *J. Am. Chem. Soc*. **76** (1954) 3047.
[13] G. M. Morris, D. S. Goodsell, R. S. Halliday, *J. Comput. Chem.* **19** (14) (1998) 1639-1662.
[14] A. T. Laurie, R. M. Jackson, *Bioinformatics* **21(9)** (2005) 1908-1916.
[15] N. M. O'Boyle, M. Banck, *J. Chem. Inform.* **3** (2011) 33.
[16] O. Trott, A. J. Olson, *J. Comput. Chem.* **31** (2010) 455-461.
[17] M. Aslanoglu, *Anal. Sci* **22** (2006) 439.
[18] N. Li, Y. Ma, C. Yang, L. Guo, X. Yan, *Biophys. Chem.* **116** (2005) 199.
[19] F. Jalali, P. S. Dorraji, *J. Pharma. Biomed. Anal.* **70** (2012) 598-601.
[20] E. Laviron, *J. Electroanal. Chem*. **101** (1979) 19-28.
[21] G. C. Zhao, J. J. Zhu, J. J. Zhang, H. Y. Chen, *Anal. Chim. Acta* **394** (1999) 337.
[22] N. Alexei, M. Pankratov, I. Uchaeva, N. A. Stepanov, *Can. J. Chem.* **71** (1993) 674-677.
[23] B. Xu, K. Jiao, Y. Ren, W. Sun, *J. Chin. Chem. Soc.* **54** (2007) 917-924.
[24] A. Shah, M. Zaheer, R. Qureshi, Z. Akhter, M. F. Nazar, *Spectrochimica Acta Part A* **75** (2010) 1082–1087.
[25] J. Jayabharathi, V. Thanikachalam, M. Venkatesh Perumal, N. Srinivasan, *Spectrochim. Acta Part A: Mol. Biomol. Spectr.* **79** (2011) 236
[26] C. Wang, Q. Chu, C. Chen, Z. Bo, *Spectroscopy* **25** (2011) 113-122.
[27] Q. Wang, X. Wang, Z. Yu, X. Yuan, K. Jiao, *Int. J. Electrochem. Sci.* **6** (2011) 5470 – 5481.

J. Electrochem. Sci. Eng. **6(2)** (2016) 165-173 ; doi: **10.5599/jese.278**

Open Access : : ISSN 1847-9286

www.jESE-online.org

Original scientific paper

Oxygen source-oriented control of atmospheric pressure chemical vapor deposition of VO_2 for capacitive applications

Dimitra Vernardou*,✉, Antonia Bei**, Dimitris Louloudakis*,***, Nikolaos Katsarakis*,****,*****, Emmanouil Koudoumas*,*****

**Center of Materials Technology and Photonics, School of Engineering, Technological Educational Institute of Crete, 710 04 Heraklion, Crete, Greece*
***Department of Mechanical Engineering, School of Engineering, Technological Educational Institute of Crete, 710 04 Heraklion, Crete, Greece*
****Department of Physics, University of Crete 711 00 Heraklion, Crete, Greece*
*****Department of Electrical Engineering, School of Engineering, Technological Educational Institute of Crete, 710 04 Heraklion, Crete, Greece*
******5Institute of Electronic Structure & Laser, Foundation for Research & Technology- Hellas, P.O. Box 1527, Vassilika Vouton, 711 10 Heraklion, Crete, Greece.*

✉Corresponding Author: dvernardou@staff.teicrete.gr

Received: March 18, 2016; Revised: May 19, 2016; Accepted: May 23, 2016

Abstract

Vanadium dioxides of different crystalline orientation planes have successfully been fabricated by chemical vapor deposition at atmospheric pressure using propanol, ethanol and O_2 gas as oxygen sources. The thick a-axis textured monoclinic vanadium dioxide obtained through propanol presented the best electrochemical response in terms of the highest specific discharge capacity of 459 mAh g^{-1} with a capacitance retention of 97 % after 1000 scans under constant specific current of 2 A g^{-1}.

Keywords

Atmospheric pressure chemical vapor deposition; O_2 source; Vanadium dioxide; Electrochemical properties.

Introduction

Vanadium dioxide (VO_2) exists in more than 10 polymorphs, however, rutile, monoclinic (described as a slightly distorted rutile structure) and metastable phases have mainly attracted interest because of their interesting chemical and physical properties for catalytic and electrochemical applications [1-3]. The crystal structure of VO_2 consists of sheets of edge-sharing

VO_6 octahedra linked by corner sharing to adjacent sheets along the c-direction of the unit cell [4]. This corner-sharing structure strengthens the structural stability and the resistance to lattice shearing during cycling in lithium ion batteries [5]. In that context, VO_2 was found to show better electrochemical performance compared with the well-known V_2O_5 [6].

To date, various VO_2 forms have been synthesized such as nanocrystalline VO_2(B) [4], nanothorn VO_2(B) hollow microspheres [7], three dimensional hierarchical microflowers and microspheres [8,9] as well as VO_2/reduced graphene oxide [10,11], VO_2(B)/carbon nanotubes [12] and hydrogen treated VO_2 [13] composite powder materials with sufficient capacitive characteristics. But, most of the above mentioned materials showed poor cycling stability after 500 cycles. Hence, it is important to improve the long-term performance and high rate capability of VO_2.

Due to the small compositional differences between numerous phases of vanadium oxides, VO_2 preparation requires a stringent controlled process that provides desired oxygen stoichiometry and crystalline structure. In search of such a process, VO_2 has been grown using sol-gel [14], pulsed laser deposition [15], sputtering [16] and chemical vapor deposition (CVD) [17-20]. Among these techniques, CVD at atmospheric pressure (APCVD) is gaining attention because it does not require expensive vacuum systems, has fast deposition rates and can be easily integrated to float-glass production lines [21-24]. A range of precursors have been utilized including vanadium(IV) chloride (VCl_4) [22], vanadyl(IV) acetylacetonate ($VO(acac)_2$) [23-24], vanadium(V) oxytrichloride ($VOCl_3$) [25], vanadium(V) triisopropoxide oxide ($VO(OC_3H_7)_3$ [26-28]. Since highly oriented VO_2 films exhibited significant variation in conductivity as thermochromic layers [29-31], we were inspired to investigate the orientation effect on the APCVD coatings for capacitive applications.

In this paper, the APCVD of VO_2 on SnO_2-precoated glass substrate was studied using $VO(acac)_2$ and propanol, ethanol, O_2 gas as oxygen sources from the perspective of the potential application of such coatings as cathodes. We have demonstrated the differences in the resulting coatings obtained from a structure-orienting role played by the oxygen sources utilized and possible explanation of this role is examined.

Experimental

Preparation of VO_2 coatings

The APCVD reactor utilized in this work was an in-house design as also reported previously [3,23,24]. The vanadium source was the $VO(acac)_2$ (98 %, Sigma-Aldrich), which was placed in a bubbler at 200 ^oC, while the gas lines were kept at 220 ^oC to avoid any condensation or blocking. The carrier gas was N_2 (99.9 %), which was passed through the reactor during all depositions. The N_2 flow rate through the vanadium precursor bubbler was 1.4 L min^{-1}, for growth temperature and period of 500 ^oC and 7.5 min, respectively. Additionally, the flow rate of propanol (99.5 %, Sigma-Aldrich), ethanol (≥ 99.5 %, Sigma-Aldrich) and O_2 gas (99.9 %) was 0.8 L min^{-1}. Finally, the total N_2 flow rate was kept at 12 L min^{-1} in all CVD experiments.

The substrates were commercial SnO_2-precoated glass (Uniglass, Greece), all of dimensions 2×2×0.4 cm. Prior to deposition, they were all cleaned with H_2O and detergent, rinsed thoroughly with H_2O and deionised H_2O, and allowed to dry in air. Once the allotted time was complete, the reactor temperature was turned off and the substrate allowed cooling at 100 ^oC under an atmosphere of N_2. Then it was removed from the reactor, handled and stored in air.

Structural and morphological characterization of coatings

The structure of the coatings was examined in a Siemens D5000 Diffractometer for 2-theta = 15.00 – 60.00 ^{o}, step size 0.05 ^{o} and step time 5 min/^{o}. Additionally, their morphology was evaluated in a Jeol JSM-7000 microscope. In this case, coatings were over-coated with a thin film of gold prior to analysis to avoid charging.

Finally, the coating's thickness was estimated using a profilometer A-step TENCOR. A step was done by etching the vanadium oxide coatings off the SnO_2-precoated glass substrate in 1:3, H_2O_2 (30 %):HCl. Tin dioxide remained intact after this procedure and the thickness was obtained from the measured step height.

Electrochemical evaluation

Cyclic voltammetry experiments were performed using a three electrode electrochemical cell as reported previously [32-34] for a potential range of -1 V to +1 V, a scan rate of 10 mV s^{-1} and a number of scans up to 1000. In particular, Pt, Ag/AgCl and vanadium oxides on SnO_2-precoated glass substrates were used as counter, reference and working electrodes, respectively. All measurements were carried out in 1 M LiOH, which acted as electrolyte. The chronoamperometric measurements were done at -1 V and +1 V for a step of 200 s and a total period of 2000 s. Additionally, the chronopotentiometric curves were obtained at a constant specific current of 2 A g^{-1} and a potential range of +0.1 V to +0.6 V.

Results and discussion

Presented here are investigations into APCVD VO_2 coatings grown from $VO(acac)_2$ and three oxygen sources: propanol, ethanol and O_2 gas. It will be shown that a level of control can be exerted over orientation and morphology through the different sources. All coatings produced were stable in air for over six months and resistant to H_2O, acetone and toluene. Additionally, they passed the "scotch tape test"; a piece of sticky tape was placed on the coating and then removed without lifting off the coating.

Structure

Figure 1 presents the x-ray diffraction (XRD) patterns of the APCVD coatings using propanol, ethanol and O_2 gas. As shown in the case of propanol and ethanol, one diffraction peak is observed at 18.21 ^{o}, which matches to monoclinic a-axis textured VO_2 coatings [30,31,35]. This peak can be indexed to 100 plane showing the preferred orientation growth of these coatings. Furthermore, the XRD pattern of the as-grown coatings using O_2 gas show two peaks at 55.4 and 57.6 ^{o} with Miller indices 022 and 220 due to monoclinic VO_2 phase indicating that is a 022-oriented single phase [36-38]. Finally, peaks at 26.5, 33.7, 37.1, 51.7 and 54.7 ^{o} with respective Miller indices 110, 101, 211 and 220 (indicated with asterisk in Figure 1) are due to SnO_2–precoated glass substrate [39]. The preferential orientation of the VO_2 on SnO_2-precoated glass substrates at angles other than 27.8 ^{o} is not clearly understood. Nevertheless, it seems to be more sensitive to O_2 source during the growth rather than to glass substrate. The reaction mechanism for the formation of VO_2 from $VO(acac)_2$ in the presence of O_2 gas has previously been studied in the literature [40]. The possible decomposition routes of $VO(acac)_2$ species involve a simple intramolecular rearrangement of the $VO(acac)_2$ precursor resulting in the release of two C_3H_4 molecules, followed by the decomposition of $VO(CH_3COO)_2$ to yield $(CH_3CO)_2O$ and VO_2. On the other hand, in the case of alcohols, the VO_2 deposits possibly act as heterogeneous catalytic sites for their oxidation to propanal (for propanol) and acetaldehyde (for ethanol). A similar behavior is also observed in the

presence of methanol [41,42]. The active oxygen required for their oxidation comes from the $VO(acac)_2$ itself, since it can be regarded as a source of excess oxygen (there are 5 oxygen atoms to 1 V atom, while only 2 oxygen atoms are required for VO_2 formation).

Other researchers have also attempted to control the crystalline orientation of VO_2. Gary et. al. reported the a-axis textured VO_2 deposited on R-plane sapphire and suggested that the cause could be a stress developing on the interface between the substrate and the coating [30]. Muraoka *et. al.* studied the epitaxial growth of VO_2 001-oriented single phase on TiO_2 001 substrates and 110-oriented phase on TiO_2 110, respectively [29]. Ngom *et. al.* indicated that the crystalline orientation of the VO_2 thin films was drastically changed because of the formation of an interface layer between the VO_2 and the soda lime glass [35]. Chiu et. al. also attempted to grow VO_2 on glass using a 5 nm ZnO buffer layer. In the case of the direct VO_2 growth on amorphous glass, polycrystalline films formed, while only VO_2 011 peaks located at 27.90 ^{o} were observed for the growth on ZnO [43].

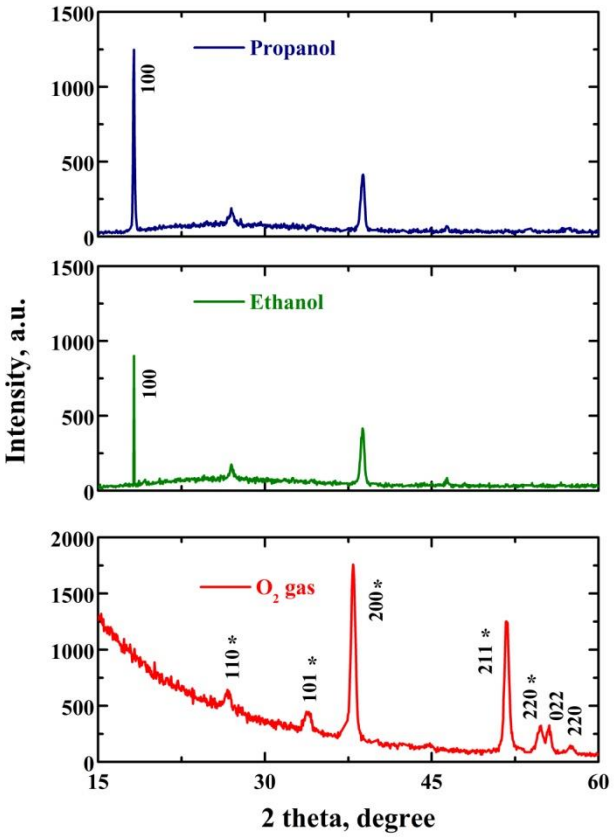

Figure 1. *XRD of APCVD vanadium oxides at 500 ^{o}C for 0.8 L min^{-1} flow rate of propanol, ethanol and O_2 gas.*

Morphology

Figure 2 presents the field-emission scanning electron microscope (FE-SEM) images of vanadium oxide coatings grown at 500 ^{o}C on SnO_2-precoated glass substrate for 0.8 L min^{-1} flow rate of propanol, ethanol and O_2 gas. For propanol and ethanol, compact grains of nearly round shape are mainly observed with their sizes being 160 nm and 40 nm, respectively. It was observed that thinner coatings grown using ethanol (95 nm) were denser, while as thickness increased for propanol (120 nm), the surface appeared less dense with growth at specific sites, suggestive of a Stranski-Krastanov type of growth mechanism [44]. Regarding the O_2 gas, agglomeration of grains forming rod-like structures is shown with thickness of 80 nm.

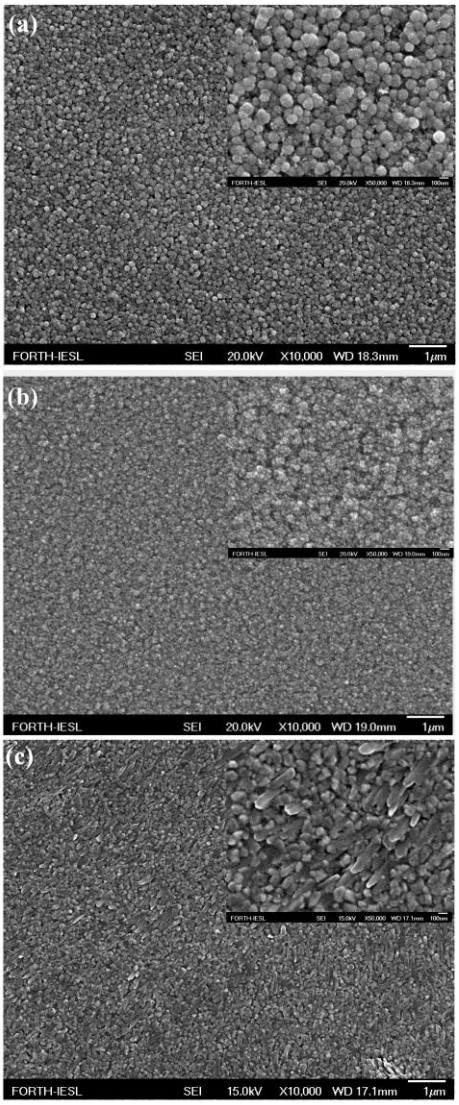

Figure 2. *FE-SEM of APCVD vanadium oxides at 500 ^{o}C for 0.8 L min^{-1} flow rate of propanol (a), ethanol (b) and O_2 gas (c).*

Electrochemical characteristics

In order to study the effect of oxygen source on the electrochemical performance of the coatings, cyclic voltammetry curves were obtained as indicated in Figure 3. The potential range was -1 V to +1 V at a scan rate of 10 mV s^{-1}. All curves are normalized to the mass of the working electrode. The mass was measured by a 5-digit analytical grade scale and found to be 0.00002 g, which was obtained by measuring the glass substrate before and after the growth. It can be observed that the as-grown vanadium oxide coatings using propanol present two anodic peaks at -0.05 V / +0.52 V and two cathodic peaks at -0.15 V / ≈+0.64 V (*vs.* Ag/AgCl), which are accompanied by color changes from green, blue to yellow and then yellow, blue to green. Since, the electrochemical cell is made up of glass, we have observed these color changes during the measurements. One may then assume that V^{+5} ions are reduced to V^{+4} and V^{+3}, since two anodic peaks are observed. A similar explanation can be given for the oxidation peaks, *i.e.* V^{+3} ions oxidize into V^{+4} and V^{+5}. These color changes are attributed to Li^{+} intercalation and deintercalation [45]. On the other hand, the shape of the curve for the vanadium oxide coating using O_2 gas is different indicating one anodic peak at +0.11 V and one cathodic peak at -0.34 V accompanied by color changes from green to yellow and vice versa. This may be due to the existence of different VO_2

orientation planes compared with the one observed for alcohols. Furthermore, the specific current of the as-grown coatings using alcohols as oxygen source is the highest presenting an enhanced electrochemical activity. We then suggest that this is correlated to both the 100 plane and the increased thickness, which incorporate more active material for the insertion of Li^+.

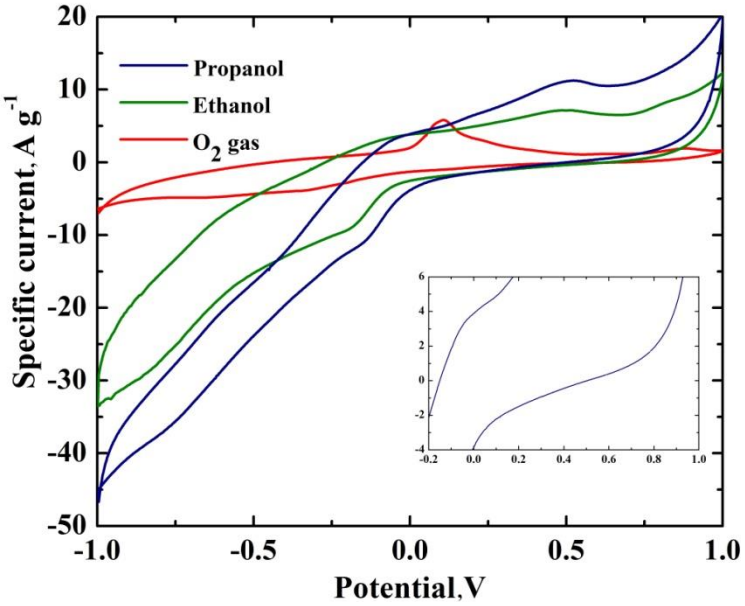

Figure 3. *Cyclic voltammograms of the first scan for the APCVD vanadium oxide coatings for 0.8 L min^{-1} flow rate of propanol, ethanol and O_2 gas and an electrode geometrical active area of 1 cm^2. Maximized cyclic voltammogram curve for the region of -0.2 V - +1 V of the grown vanadium oxide coating using propanol as inset.*

Chronoamperometry measurements were also performed to calculate the specific charge during Li^+ intercalation / deintercalation. It is estimated by integration of excess current measured upon switching the bias potential with time [32] as shown in Figure 4 for the as-grown vanadium oxide using 0.8 L min^{-1} of propanol. The amount of specific charge for propanol found to be 120 C g^{-1}, which is three times higher than that of O_2 gas.

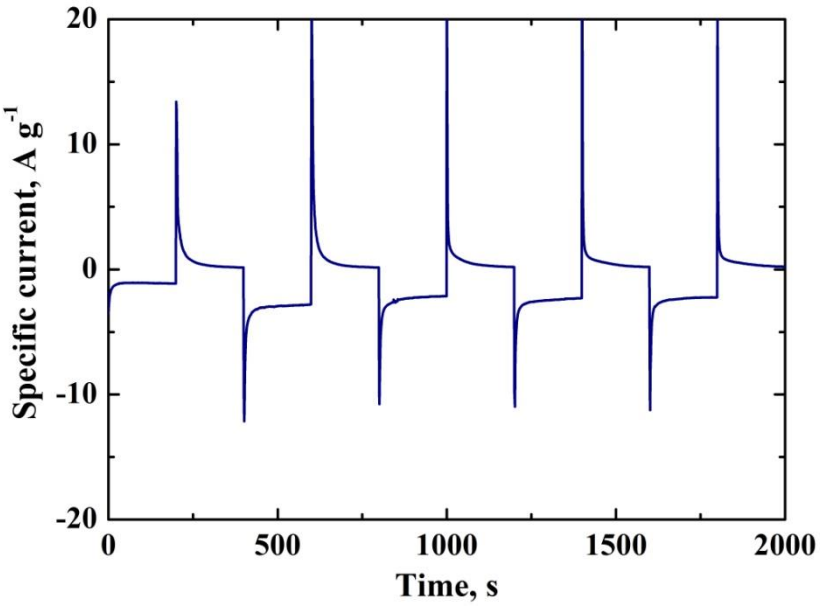

Figure 4. *The chronoamperometric response of the first scan recorded at -1 V and +1 V for an interval of 200 s of the as-grown coatings at 500 ^oC for 0.8 L min^{-1} flow rate of propanol.*

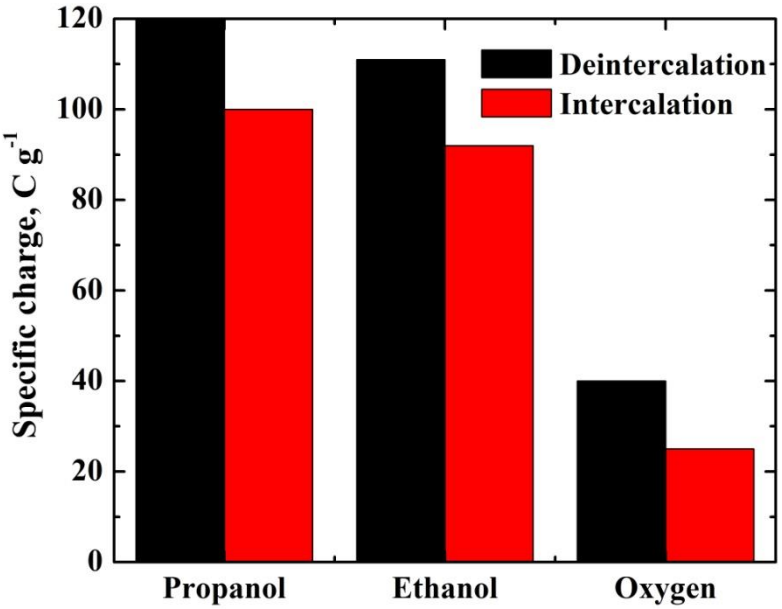

Figure 5. *Intercalated and deintercalated specific charge as a function with oxygen source utilized.*

Figure 6 presents the specific discharge capacities of the as-grown coatings at 500 ^{o}C for 7.5 in using 0.8 L min^{-1} flow rate of propanol, ethanol and O_2 gas under a constant specific current of 2 A g^{-1}. The propanol's curve indicates two plateaus at approximately 0.25 V and 0.5 V, which present the two-step Li^+ intercalation process as also observed in cyclic voltammetry analysis. The specific discharge capacity was 459 mAh g^{-1} with a capacitance retention of 97 % after 1000 scans (Figure 6 inset) keeping the staircase shape, which is promising for lithium ion batteries. The specific discharge capacity was higher than the APCVD metastable [3] and 022-oriented monoclinic VO_2 [24]. On the other hand, the ethanol and O_2 gas samples lack of staircase-like shape probably due to the less defined phase transition associated with Li^+. This result may arise due to the largest thickness of the propanol sample, which facilitates larger number of Li^+ within the vanadium oxide lattice.

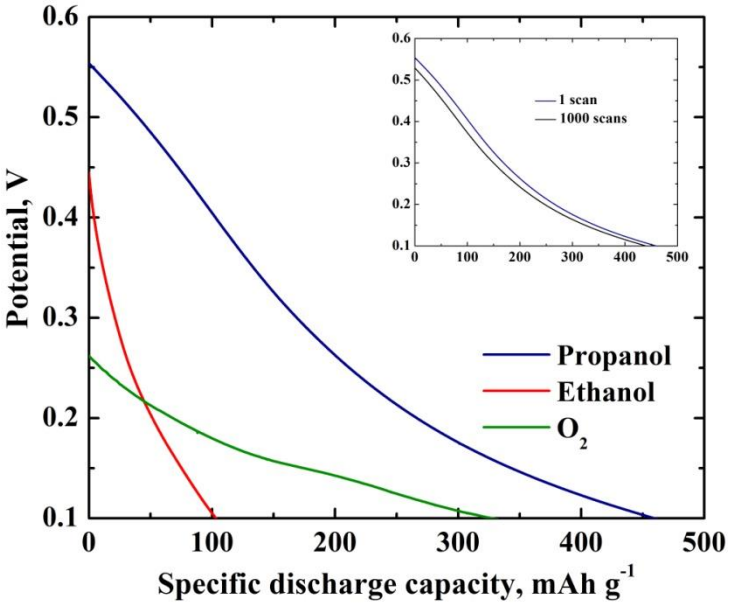

Figure 6. *The chronopotentiometric curves for the as-grown sample at 500 ^{o}C for 7.5 min using 0.8 L min^{-1} propanol, ethanol and O_2 gas under a constant specific current of 2 A g^{-1} and potential ranging from 0.1 V to 0.6 V. The 1000th scan of 0.8 L min^{-1} propanol is also included as inset.*

Conclusions

Vanadium dioxides of different crystalline orientation were grown by APCVD at 500 ^{o}C for 7.5 min using propanol, ethanol and O_2 gas. The a-axis textured monoclinic was enhanced with propanol and ethanol, while the 022-oriented single phase VO_2 was obtained with O_2 gas. Consequently, the samples with different orientations possessed different morphologies; a-axis textured coatings showed grains, while the 022-oriented phases presented agglomeration of grains forming rod-like structures. Electrochemical analysis has shown that the a-axis textured monoclinic VO_2 grown using propanol has several unique characteristics compared with the rest of the samples, which makes it promising electrode material for lithium ion batteries. These include the thickness, which facilitates Li^+ access to a large volume of active material and the specific discharge capacity of 459 mAh g^{-1} with capacitance retention of 97 % after 1000 scans under constant specific current of 2 A g^{-1} indicating both high rate performance and good stability.

References

[1] M. Rahman, J. Z. Wang, N. H. Idris, Z. Chen, H. Liu, *Electrochim. Acta* **56** (2010) 693-699.
[2] C. V. Subba Reddy, E. H. Walker Jr., S. Wicker Sr., Q. L. Williams, R. R. Kalluru, *Curr. Appl. Phys.* **9** (2009) 1195-1198.
[3] D. Vernardou, D. Louloudakis, E. Spanakis, N. Katsarakis, E. Koudoumas, *Int. J. Thin Film Sci. Tech.* **4** (2015) 187-191.
[4] E. Baudrin, G. Sudant, D. Larcher, B. Dunn, J. M. Tarascon, *Chem. Mater.* **18** (2006) 4369-4374.
[5] F. Wang, Y. Liu, C. Liu, *Electrochim. Acta* **55** (2010) 2662-2666.
[6] Y. Shi, S. -L. Chou, J. -Z. Wang, H. -J. Li, H. -K. Liu, Y. -P. Wu, *J. Power Sources* **244** (2013) 684-689.
[7] H. M. Liu, Y. G. Wang, K. X. Wang, E. Hosono, H. S. Zhou, *J. Mater. Chem.* **19** (2009) 2835-2840.
[8] H. Liu, Y. Wang, L. Li, K. Wang, E. Hosono, H. Zhou, *J. Mater. Chem.* **19** (2009) 7885-7891.
[9] S. Zhang, Y. Li, C. Wu, F. Zheng, Y. Xie, *J. Phys. Chem. C* **113** (2009) 15058-15067.
[10] L. Deng, G. Zhang, L. Kang, Z. Lei, C. Liu, Z. -H. Liu, *Electrochim. Acta* **112** (2013) 448-457.
[11] H. Wang, H. Yi, X. Chen, X. Wang, *J. Mater. Chem. A* **2** (2014) 1165-1173.
[12] L. Liang, H. Liu, W. Yang, *J. Alloys Compd.* **559** (2013) 167-173.
[13] X. Pan, Y. Zhao, G. Ren, Z. Fan, *Chem. Commun.* **49** (2013) 3943-3945.
[14] I. P. Parkin, R. Binions, C. Piccirillo, C. S. Blackman, T. D. Manning, *J. Nano Res.* **2** (2008) 1-20.
[15] M. Maaza, K. Bouziane, J. Maritz, D. S. McLachlan, R. Swanepool, J. M. Frigerio, M. Every, *Opt. Mater.* **15** (2000) 41-45.
[16] J. B. K. Kana, J. M. Ndjaka, P. O. Ateba, B. D. Ngom, N. Manyala, O. Nemraoui, A. C. Beye, M. Maaza, *Appl. Surf. Sci.* **254** (2008) 3959-3964.
[17] C. L. Choy, *Prog. Mater. Sci.* **48** (2003) 57-170.
[18] M. B. Sahana, M. S. Dharmaprakash, S. A. Shivashankar, *J. Mater. Chem.* **12** (2002) 333-338.
[19] M. B. Sahana, S. A. Shivashankar, *J. Mater. Res.* **19** (2004) 2859-2870.
[20] M. N. Field, I. P. Parkin, *J. Mater. Chem.* **10** (2000) 1863-1866.
[21] T. D. Manning, I. P. Parkin, M. E. Pemble, D. Sheel, D. Vernardou, *Chem. Mater.* **16** (2004) 744-749.
[22] D. Vernardou, M. E. Pemble, D. W. Sheel, *Thin Solid Films* **515** (2007) 8768-8770.
[23] D. Vernardou, M. E. Pemble, D. W. Sheel, *Chem. Vapor Depos.* **12** (2006) 263-274.
[24] D. Vernardou, M. Apostolopoulou, D. Louloudakis, N. Katsarakis, E. Koudoumas, *Chem. Vapor Depos.* **21** (2015) 1-3.

[25] T. D. Manning, I. P. Parkin, *Polyhedron* **23** (2004) 3087-3095.
[26] L. Kritikos, L. Zambelis, G. Papadimitropoulos, D. Davazoglou, *Surf. Coat. Tech.* **201** (2007) 9334-9339.
[27] S. Mathur, T. Ruegamer, I. Grobelsek, *Chem. Vap. Deposition* **13** (2007) 42-47.
[28] D. Vernardou, D. Louloudakis, E. Spanakis, N. Katsarakis, E. Koudoumas, *Sol. Energ. Mat. Sol. C.* **128** (2014) 36-41.
[29] Y. Muraoka, Z. Hiroi, *Appl. Phys. Lett.* **80** (2002) 583-585.
[30] G. Garry, O. Durand, A. Lordereau, *Thin Solid Films* **453** (2004) 427-430.
[31] Y. Zhang, R. Wang, Z. Qiu, X. Wu, Y. Li, *Mater. Lett.* **131** (2014) 42-44.
[32] D. Vernardou, M. Apostolopoulou, D. Louloudakis, N. Katsarakis, E. Koudoumas, *J. Colloid Interf. Sci.* **424** (2014) 1-6.
[33] D. Vernardou, A. Sapountzis, E. Spanakis, G. Kenanakis, E. Koudoumas, N. Katsarakis, *J. Electrochem. Soc.* **160** (2013) D6-D9.
[34] D. Vernardou, M. Apostolopoulou, D. Louloudakis, E. Spanakis, N. Katsarakis, E. Koudoumas, J. McGrath, M.E. Pemble, *J. Alloy. Compd.* **586** (2014) 621-626.
[35] B. D. Ngom, M. Chaker, A. Diallo, I. G. Madiba, S. Khamlich, N. Manyala, O. Nemraoui, R. Madjoe, A. C. Beye, M. Maaza, *Acta Mater.* **65** (2014) 32-41.
[36] X. Wu, Y. Tao, L. Dong, Z. Wang, Z. Hu, *Mater. Res. Bull.* **40** (2005) 315-321.
[37] J. Shi, S. Zhou, B. You, L. Wu, *Sol. Energ. Mat. Sol. C* **91** (2007) 1856-1862.
[38] J. B. Kana Kana, J. M. Ndjaka, B. D. Ngom, N. Manyala, O. Nemraoui, A. Y. Fasari, R. Nemutudi, A. Gibaud, D. Knoesen, M. Maaza, *Thin Solid Films* **518** (2010) 1641-1647.
[39] E. Elangovan, K. Ramamurthi, *Thin Solid Films* **476** (2005) 231-236.
[40] D. Vernardou, M. E. Pemble, D. W. Sheel, *Thin Solid Films* **516** (2008) 4502-4507.
[41] G. I. N. Waterhouse, G. A. Bowmaker, J. B. Metson, *Appl. Catal. A Gen.* **266** (2004) 257-273.
[42] P. Forzatti, E. Tronconi, A. S. Elmi, G. Busca, *Appl. Catal. A Gen.* **157** (1997) 387-408.
[43] T. –W. Chiu, K. Tonooka, N. Kikuchi, *Thin Solid Films* **518** (2010) 7441-7444.
[44] M. Ohring, *The Materials Science of Thin Films*, Academic Press, London, 1992.
[45] K. Lee, G. Cao, *J. Phys. Chem. B* **109** (2005) 11880-11885.
[46] D. Vernardou, I. Marathianou, N. Katsarakis, E. Koudoumas, I. I. Kazadojev, S. O' Brien, M. E. Pemble, I. M. Povey, *Electrochim. Acta* **196** (2016) 294-299.
[47] J. Qin, W. Lv, Z. Li, B. Li, F. Kang, Q. –H. Yang, *Chem. Commun.* **50** (2014) 13447-13450.
[48] Y. Wu, P. Zhu, X. Zhao, M. V. Reddy, S. Peng, B. V. R. Chowdari, S. Ramakrishna, J. *Mater. Chem. A* **1** (2013) 852-859.

J. Electrochem. Sci. Eng. **6(2)** (2016) 175-185; doi: **10.5599/jese.279**

Open Access : : ISSN 1847-9286

www.jESE-online.org

Original scientific paper

Anticorrosive behaviour of lumefantrine hydrophobic layer on mild steel surface

Pavithra M. Krishnegowda, Venkatesha T. Venkatarangaiah ✉,
Punith Kumar M. Krishnegowda*, Anantha N. Subba Rao, Shubha H. Nataraj

Department of Chemistry, Kuvempu University, Shankaraghatta-577451, Shimoga, Karnataka, India
**Department of Materials Engineering, Indian Institute of Science, Bangalore-560012, Karnataka, India*

✉Corresponding Author: drtvvenkatesha@yahoo.co.uk; Tel.: +91-9448855079

Received: March 22, 2016; Revised: May 17, 2016; Accepted: May 18, 2016

Abstract

The surface modification of mild steel was achieved by chemical treatment in lumefantrine (LF) solution. The surface morphology and wettability of modified surface was analysed by 3D profilometer and contact angle goniometer. The corrosion inhibition performance of modified mild steel surface in 1.0 M HCl solution was investigated by potentiodynamic polarization and electrochemical impedance techniques.Electrochemical measurements illustrate that the corrosion of mild steel in acidic chloride medium get substantially reduced by introducing LF film on its surface (94 % efficiency). Quantum chemical parameters were evaluated by ab initio method and they confer appropriate theoretical support to the experimental findings.

Keywords

Acid solutions; Mild steel; Polarization; Electrochemical impedance spectroscopy ;Acid corrosion

Introduction

The service life of metals can be improved by their surface modification using electroactive compounds [1]. Organic molecules containing O, N, S and polar functional groups are the extensively used electro active compounds, owing to their strong adsorption tendency on the metal surface. These electro active compounds form a thin film or molecular layers on the metal surface. Traditionally, hetero aromatic compounds have been used for mild steel (MS) protection [2-7]. However, these compounds are harmful to the environment due to their toxicity. Therefore, it

becomes important to search for new, nontoxic and effective organic compounds to serve the same purpose. In this regard, drugs are the promising alternatives, referred as green corrosion inhibitors [8,9]. Drug molecules have been used for the corrosion inhibition of MS in different corrosive media and remarkable results have been reported [10-14]. In the present work, the antimalarial drug 'Lumefantrine' has been selected to protect the MS from corrosion in acidic chloride medium.The MS was chemically treated with $CHCl_3$ solution containing lumefantrine (LF) and the corrosion behaviour of modified mild steel (MMS) surface was examined by electrochemical techniques.

Experimental

Materials and sample preparation

The experiments were performed with MS specimens having composition 0.04 % C, 0.35 % Mn, 0.022 % P, 0.036 % S, and the remainder being Fe. The MS coupons of1 cm^2 area (exposed) with a 5 cm long stem isolated with araldite resin were used for electrochemical measurements. Prior to each experiment, the metal samples were abraded with series of emery papers (grade No. 220, 660 and 1200) followed by thorough wash using millipore water, acetone and then dried in hot air.

The aggressive solution of 1.0 M HCl was prepared from AR grade 37 % HCl and millipore water. The millipore water was obtained from Elix 3 Milli-pore system (Resistivity greater than 18 MΩ cm at 25 ^oC). Lumefantrine was obtained from Ramdev Chemicals India Pvt. Ltd., Mumbai and its structure is as shown in Figure 1. The different concentrations of $CHCl_3$ solutions of LF were prepared by dissolving desired amount of LF in $CHCl_3$. The MS coupons were dipped in 100 ml of $CHCl_3$ solutions of LF for about 1 hr to obtain MMS. After surface modification, the metal samples were dried and stored in desiccator for further corrosion studies. The MS coupon modified in 3mM LF solution was used for surface analyses.

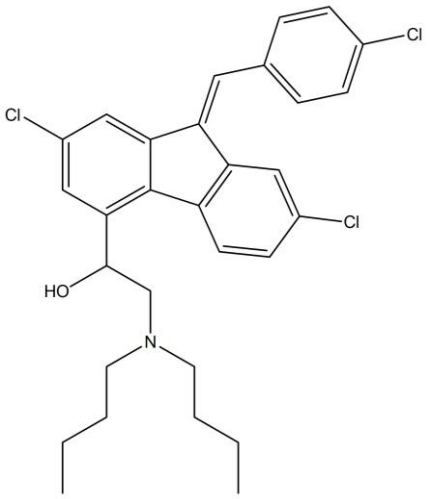

Figure 1. *Structure of lumefantrine*

Contact angle measurement

An OCA 30 from DataPhysics Instruments GmbH, Germany was used to measure the contact angles. The contact angle of water on the metal sample was measured by the sessile drop method. A commercial goniometer was used with the volumes of water droplets fixed at 2 µL and the measurements were performed at room temperature.Images of the Air/Liquid/Solid (A/L/S) systems were captured and processed using the 32-bit SCA 20 software.

Infrared spectra

An infrared reflection absorption spectroscopy (GX spectrometer, Perkin Elmer, U.S.A.) instrument outfitted with a liquid nitrogen cooled mercury cadmium telluride (MCT) detector was used to take IR spectra. Before starting the experiments the sample and detector chambers were purged with nitrogen gas. The reported IR spectra were obtained with reference to bare steel substrate over 1024 optimized scans at 4 cm^{-1} resolution by using polarized beam spectra of modified surface.

The surface morphology

The surface of MS samples was examined by Zeta-20 True Color 3D Optical Profiler (Zeta Instruments, CA, U.S.A.). After the experiment, the metal samples were kept in a vacuum desiccator and were mounted on sample holder under the objective of the Optical Profiler, and the 2D photos were taken from the 50× magnified surface.

Quantum chemical studies

Quantum chemical calculations were performed using standard HyperChem, Release 8.0 software (Hypercube, Inc. GmBH Austria, USA). Geometrical structure of LF molecule was optimized by parametric (PM3) method. The optimized structure which has minimum energy value was used as the input structure for the geometrical optimization using ab initio method (Hartree–Fock method, 6-31G** basis set). The Polak–Rieberre algorithm which is fast and accurate was used for computation. The energy parameters in the form of root mean square gradient were kept at 0.1 kcal/Å mol. 0.1 kcal/Å mol.

Electrochemical measurements

Electrochemical measurements were conducted in a conventional glass cell using CHI 660C electrochemical analyzer (CH Instruments, Austin, TX, USA). MS specimen (1 cm^2), a platinum electrode and Ag/AgCl electrode were used as working, auxiliary, and reference electrodes respectively. Prior to each electrochemical measurement, a stabilization period of 30 min was allowed to establish a steady state open circuit potential (OCP). Each experiment was carried out in triplicate and the average values of corrosion parameters are reported.

The potentiodynamic polarization (PDP) measurements were carried out over a potential range of −200 mV to +200 mV at OCP with a scan rate of 0.5 mV s^{-1}. The corrosion kinetic parameters such as corrosion potential (E_{corr}), corrosion current density (I_{corr}), and anodic (β_a), and cathodic (β_c) Tafel slopes were evaluated by the software installed in the instrument.

The percentage inhibition efficiency η_T / %was computed from I_{corr} values using the following expression;

$$\eta_T / \% = \frac{I^o_{corr} - I_{corr}}{I^o_{corr}} \times 100 \quad (1)$$

whereI^o_{corr}andI_{corr} are the corrosion current densities without and with inhibitor, respectively.

The electrochemical impedance spectroscopy (EIS) measurements were carried at OCP in the frequency range 1 mHz to 100 kHz with 5 mV sine wave as the excitation signal. Impedance data were analyzed using ZSimp-Win 3.21 software.

The inhibition efficiency η_Z/ % was evaluated from charge transfer resistance (R_{ct}) values using the following equation

$$\eta_Z / \% = \frac{R_{ct} - R^{o}_{ct}}{R_{ct}} \times 100 \quad (2)$$

whereR^{o}_{ct} and R_{ct} are the charge transfer resistances without and with inhibitor, respectively.

Results and discussion

Morphology and contact angle measurement

The 3D profilometer images and contact angle of a water droplet (2 µL) on the naked MS surface and MMS surface are presented in Figure 2. In general, low contact angle represents the hydrophilic surface and high contact angle represents the hydrophobic surface [15-16]. In the present study, the contact angle of the naked MS is 77.15 ° (Figure 2a) and that of LF covered MS is 92.9 ° (Figure 2b). This indicate that the LF modified MS surface is more hydrophobic than the bare MS surface. Moreover, the noticeable change in contact angle value on MMS may be due to the formation of a well packed layer of LF molecules. The compact layer on MMS may be attributable to the adsorption of differently oriented LF molecules on different sites of MS surface, which affords a barrier effect against the diffusion of chloride ions [17]. On the other hand, the surface of polished MS is comparatively rough and the smooth surface of MMS may be due to the uniform coverage of LF molecules. Thus, the surface morphology and contact angle measurements substantiates the formation of LF film on the MS surface.

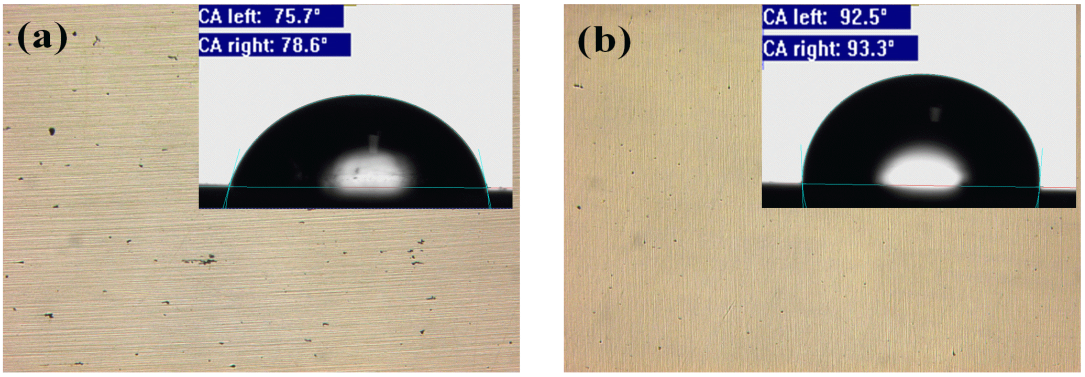

Figure 2.*Profilometer images and optical micrographs of a water dropleton (a) the naked mild steeland (b) modified mild steel.*

IR spectral analysis

The IR spectra were used to determine the presence of LF film on the modified MS surface and are depicted in Figure 3.By comparing Figure 3a and 3b,it can be observed that certain peaks have been disappeared completely and some have been shifted. Figure 3a shows the IR spectrum of LF molecule. The characteristic bandat 3490 cm^{-1} and 1459 cm^{-1} wereattributed to stretching vibration of the O-Hand aromatic C=C groups, 1151 cm^{-1}corresponds to C-N bond, 2864 cm^{-1} corresponds to aromatic and 2953 cm^{-1} corresponds to aliphatic C-H stretching. Also the band at 874 cm^{-1} is attributed to C-Cl stretching. The IR spectrum of LF film on MMS is shown in Figure 3b. In this spectrum, C-N stretching frequency is shifted to 1122 cm^{-1}, and aromatic C=C stretching frequency is shifted to 1409 cm^{-1}. Furthermore, the O-H band at 3490 cm^{-1} gets disappeared in Figure 3b. Based on these observations, it can be concluded that the adsorption of LF molecule on MS surface takes place through C=C, O-H and C-N bonds and confirms the adsorption of LF molecules on the MS surface.

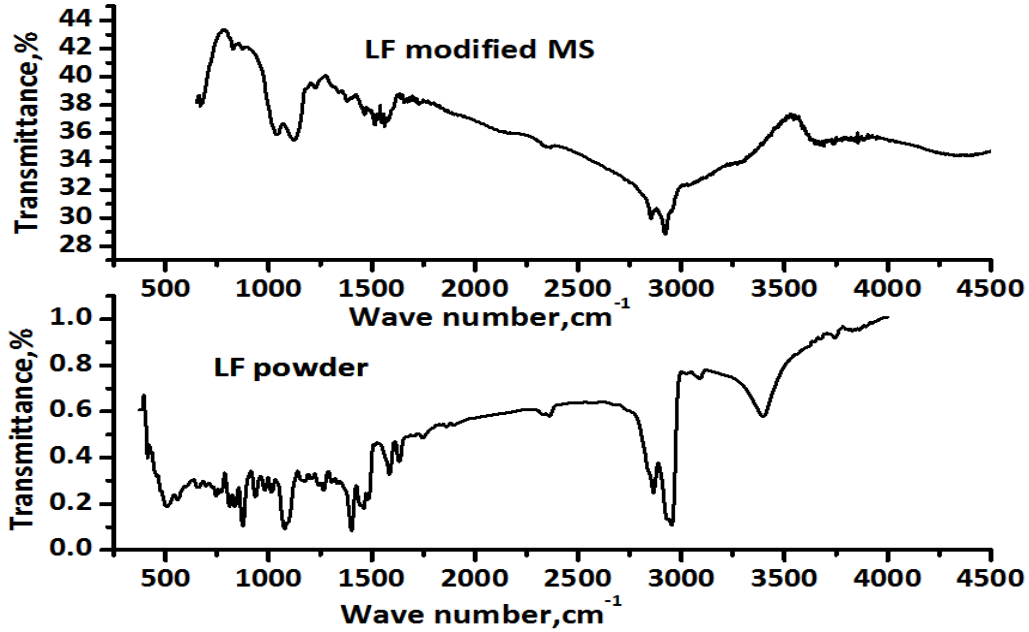

Figure 3. *IR spectra of (a) LF powder and (b) LF film on the mild steel surface.*

Quantum chemical Study

Quantum chemical calculations will provide information about the molecular structure of LF molecule responsible for the formation of film on the MS surface.The quantum chemical calculations were carried out with the help of complete geometry optimization by ab initio method using 6-31G** basis set. The geometry of LF molecule was optimized by Hartree–Fock method and the optimized structure, distribution of highest occupied molecular orbitals (HOMO) and lowest unoccupied molecular orbitals LUMO are shown in Figure 4. The calculated quantum chemical parameters are presented in Table 1.

Table1*. Quantum chemical parameters of LF*

Quantum chemical parameters	
E_{HOMO} / eV	–8.009
E_{LUMO} / eV	1.525
ΔE / eV	9.534
μ / D	4.495
Total energy, k cal mol^{-1}	–1670734.09

The spatial orbitals are distributed randomly on O, N and phenyl rings present in the molecule. Moreover, LF molecule possesshigh dipole moment (μ) and the low energy gap (ΔE) values which indicate that electron transfer from LF to the surface takes place during the process of adsorption. Conversely, the adsorption centers of organic molecules can be approximated by net atomic charges in the molecule. The net atomic charges of some atoms present in LF molecule are given in Table 2. The regions of highest electron density on organic molecule are the most plausible sites of adsorption [18,19]. Therefore, N, O and some C atoms are the active centers, which have the strongest ability to bond to the metal surface. Thus, oxygen atom, nitrogen atom and π electrons in the phenyl ring are the main active sites of adsorption on MS surface. By reviewing these

findings, it can be deduced that LF forms a compact film by the process of adsorption on the surface of MS. As a result, the above experimental findings of IR spectral analysis are in good agreement with the quantum chemical results.

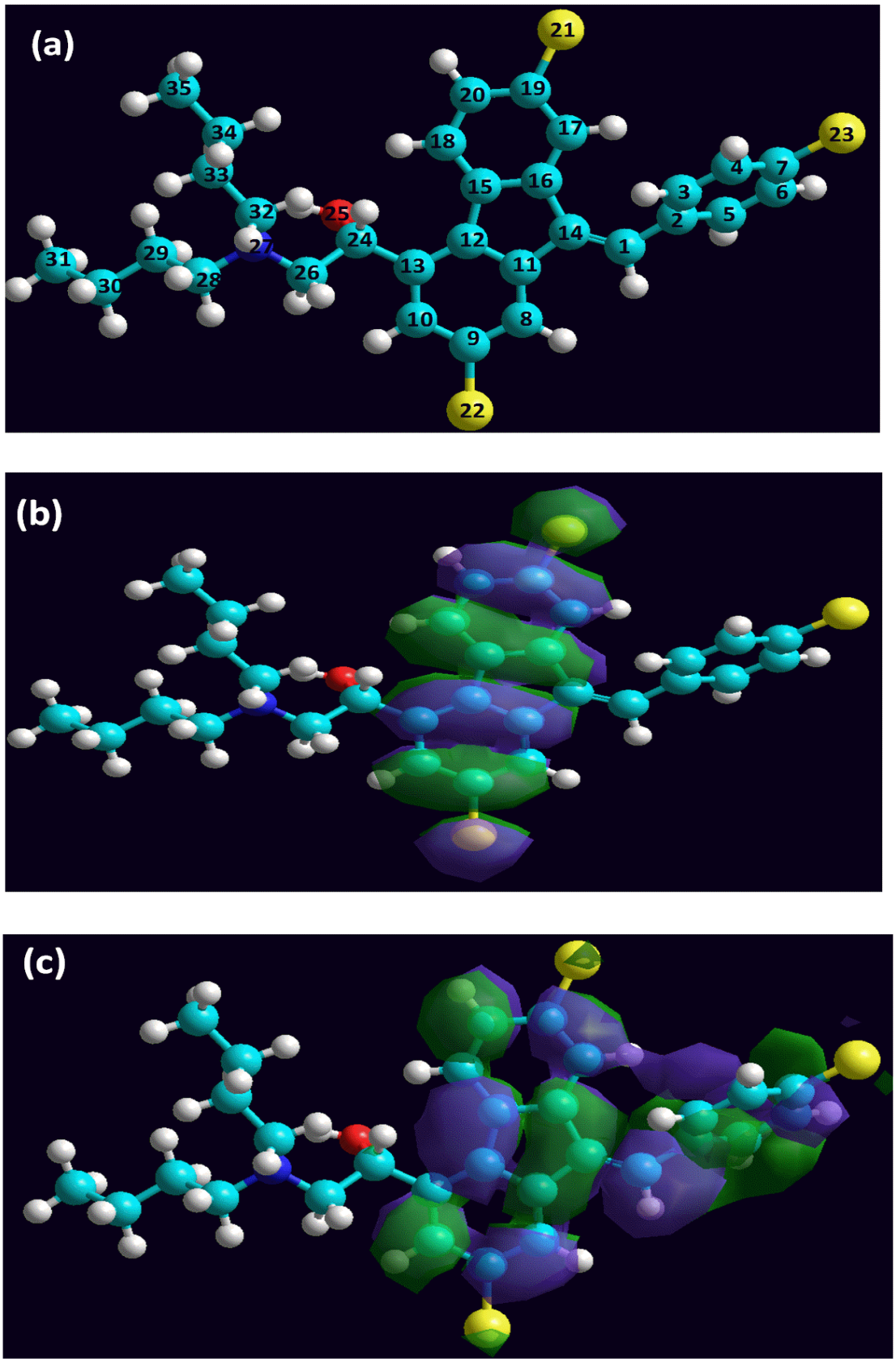

Figure 4.*(a) Optimized structure, (b) distribution ofHOMOand (c) distribution of*LUMO of LF molecule.

Table 2.*List of atoms having highest electron density in LF molecule.*

Atom	Charge
C (2)	-0.013
C (3)	-0.026
C (5)	-0.026
C (18)	-0.025
Cl (21)	-0.116
Cl (22)	-0.116
Cl (23)	-0.116
O(25)	-0.386
N (27)	-0.301
C (29)	-0.041
C (30)	-0.055
C (31)	-0.065
C (33)	-0.041
C (34)	-0.055
C (35)	-0.065

Potentiodynamicpolarisation measurements

Electrochemical analyses were performed to investigate the kinetics of electrode processes as well as the surface characteristics of the electrochemical system. The potentiodynamic polarization curves in 1M HCl for the naked MS and MMS in different concentrations of LF solutions are given in Figure 5. The electrochemical corrosion parameters such as corrosion potential (E_{corr}), corrosion current density (I_{corr}) , anodic tafel slope (β_a), cathodic tafel slope (β_c) and inhibition efficiency (η_T/ %) are tabulated in Table 3 .

It is apparent from Figure 5 that increasing the LF concentration reduces both the cathodic and anodic current densities and the E_{corr} get slightly shifted towards the anodic direction. Moreover, the decrease in both the anodic and cathodic current densities enumerated that the LF film formed on the MMS surface suppressed both the anodic and cathodic reactions [20]. This phenomenon may be due to the adsorption of the LF molecules, which in turn decreased the attack of chloride ions on the MS surface.

Table 3.*Polarization parameters in 1 M HCl for the bare mild steel and modified mild steel in different concentrations of LF solutions.*

c/mM	$-E_{corr}$/ mV	$-\beta_c$/ mV dec^{-1}	β_a / mV dec^{-1}	I_{corr}/ µA cm^{-2}	η_T/ %
0.00	449	106.46	84.38	257.5	
0.50	376	157.28	64.71	43.67	83
0.75	370	148.77	71.03	30.89	88
1.00	373	142.07	63.38	17.41	93
3.00	365	154.30	60.75	14.58	94
5.00	364	143.97	56.27	19.15	92

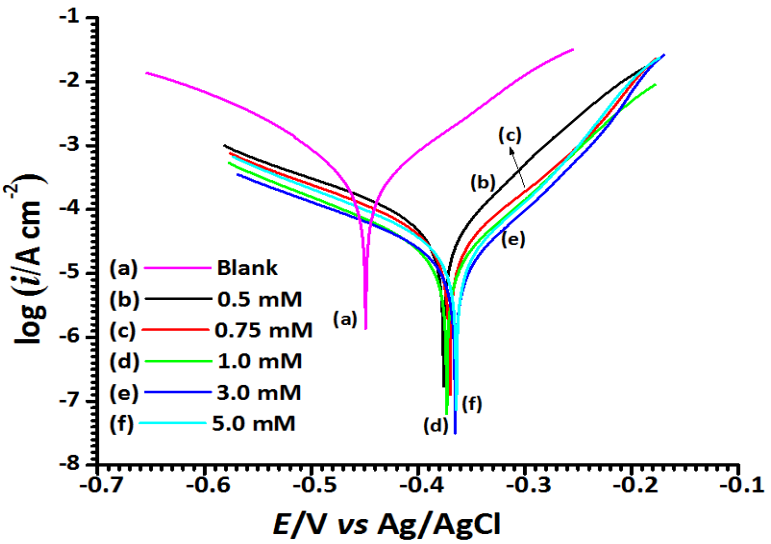

Figure 5. *Potentiodynamic polarization curves in 1 M HCl for the naked mild steel and mild steel modified inpresence of different concentrations of LF.*

It is apparent from the Table 3 that with increasing concentration of LF, I_{corr} values lowered to its minimum value at 3 mM and the η_T reached the maximum value 94 %. This implies that the film formed on the MS becomes denser with increase in LF concentration from 0.5 to 3 mM. But the η_T value decreases when the LF concentration is 5 mM. This may be due to the fact that the LF molecules get rearranged on the MS surface after the number of adsorbed molecules reaches a maximum value [21]. This makes easy for the acidic chloride ions to attack the MS surface through the interspaces. Furthermore, the values of β_a and β_c change with increase in inhibitor concentration and it indicates that the film inhibits both the anodic and cathodic reactions. By reviewing all these results it can be considered that the LF layer acts as a good protective film.

Electrochemical Impedance spectroscopy measurements

The Nyquist and Bode plots of the bare MS and LF covered MS in 1M HCl are given in Figure 6. For the naked MS, the impedance data were analyzed by the electrochemical equivalent circuit shown in the inset of Figure 6a. In this circuit, R_s represents the solution resistance, R_1 is the charge transfer resistance corresponding to the corrosion reaction at the MS/solution interface, and CPE_1 represents the constant phase element (*CPE*) as a substitute for the double-layer capacitance (C_{dl}). The impedance of *CPE* is defined as

$$Z_{CPE} = Q^{-1}(j\omega)_{-n} \quad (3)$$

where Q is the CPE constant, ω is the angular frequency, $j^2 = -1$ is the imaginary number and n is the CPE exponent which gives details about the degree of surface inhomogeneity resulting from surface roughness, inhibitor adsorption, porous layer formation etc.

For the bare MS, the Nyquist plot is the slightly depressed capacitive loop (Figure 6a) which indicates the roughness and other inhomogeneity of the MS surface [22]. The Nyquist and bode plots for MMS in different concentration of LF solutions were fitted by the equivalent circuit shown in Figure 7(a). R_s, R_1, and CPE_1 have the same meaning of elements in Figure 7a. In addition, R_2 represents the membrane resistance, which reflects the protective property of the film and CPE_2 is the capacitance of the film formed on MS [23-24]. The obtained impedance data are tabulated in Table 4.

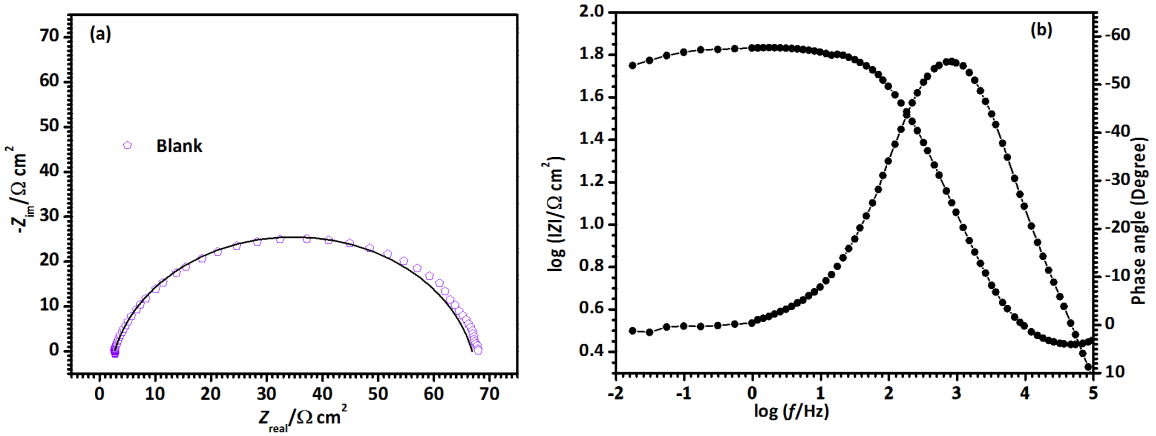

Figure 6. *(a) Nyquist plot and (b) Bode plot of naked MS in 1 M HCl*

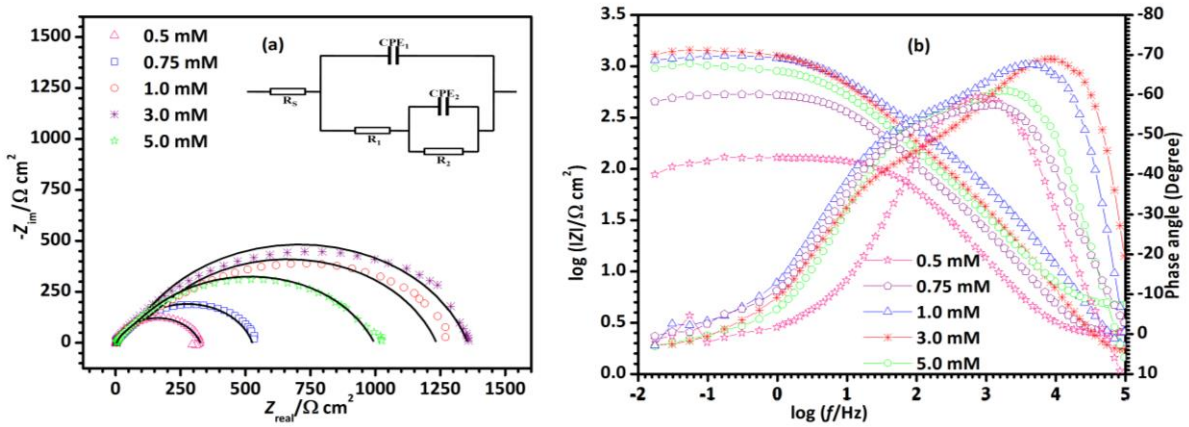

Figure 7. *EIS results in 1 M HCl for LF covered mild steel modified in differentconcentration of LF solutions: (a) Nyquist plots; (b) Bode plots*

Table 4.*Impedance parameters in 1 M HCl for the naked mild steel and mild steel modified in presence of different concentrations of LF solutions.*

c/ mM	R_1/ Ω cm^2	Q_1/ μΩ^{-1} S^n cm^{-2}	n_1	R_2/ Ω cm^2	Q_2/ μΩ^{-1} S^n cm^{-2}	n_2	η_z/ %
0.00	64.14	56.26	0.856	--	--	--	
0.50	303.5	109.4	0.733	21.1	19.38	0.999	79
0.75	499.3	51.68	0.829	24.95	17.16	0.954	87
1.00	1136	34.93	0.730	98.02	64.51	0.921	94
3.00	1292	37.84	0.815	61.75	11.20	0.946	95
5.00	950.2	59.65	0.761	41.58	33.71	0.883	93

It is apparent from Figure 7a that, the diameter of the capacitive loop increased to its maximum when the concentration of LF solution was 3 mM, implying that the compact film is formed on the surface of MS in this concentration. Bode plot shows two overlapped phase maxima, indicating the model of two time constants and the Z modulus increases with the increase of LF concentration within 3 mM, suggesting that a dense film formed on the MS exhibit better protection efficiency. It is evident that the diameter of the capacitive loop and the logarithm of Z modulus decreases when the concentration of LF is 5 mM.The inhibition efficiency calculated from R_1 also increases with increase in LF concentration, and reaches maximum (95 %) at 3 mM concentration. This may be due to the hydrophobic film of LF molecules on MS surface which inhibited the dissolution

reactions of MS to a greater extent in 1 M HCl. The variation in R_1 values imply that the corrosion reaction on the MS surface was inhibited by the absorbed inhibitor film.

Surface morphology

Morphologies of metal samples were analysed by the true color images obtained from 3D profilometer. The true color images of bare MS and MMS immersed in 1M HCl is shown in Figure 8. The surface of bare MS is completely damaged with large number of pits due to the attack of aggressive chloride ions. But MMS retains smoother surface owing to the presence of LF film which inhibits the process of corrosion in acidic chloride medium. Hence it can be concluded that, the film formed by the adsorption of LF molecules behaves as a barrier and retards MS corrosion in HCl media.

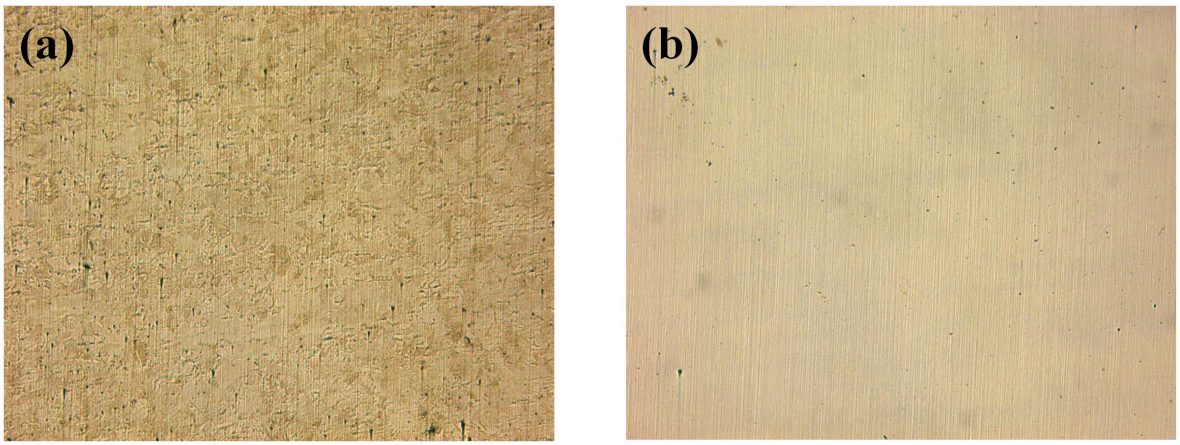

Figure 8.*Profilometer images of (a) the naked mild steel and (b) modified mild steel after immersion in 1 M HCl for 1 h.*

Conclusion

The contact angle and IR analyses indicate the presence of LF molecules on mild steel surface. The quantum chemical study reveals that the O, N and π electrons in the LF molecule are the main active sites for adsorption. The chemical treatment of MS for about 1 h leads to the formation of compact film of LF molecules and hampers acid corrosion. The LF film inhibits anodic and cathodic reactions of MS in 1 M HCl. The electrochemical studies and profilometer images confirmed the MS corrosion inhibition ability of LF molecules in acidic chloride solution.

Acknowledgement: *The authors are grateful to the authorities of Department of Chemistry, Kuvempu University, Karnataka, India for providing lab facilities. Authors also thank Department of Science and Technology, New Delhi, Govt. of India [DST: Project Sanction No. 100/IFD/1924/2008-2009 dated 2.07.2008] for providing instrumental facilities. The authors are also gratified to University Grant Commission, New Delhi, Govt. of India [UGC grant Ref. 41-231/2012(SR) dated 16.07.2012] for providing HyperChem software facility.*

References

[1] T.T.Qin, J. Li, H.Q. Luo, M. Li, N.B. Li, *Corros. Sci.***53** (2011) 1072–1078.
[2] Q.Q. Liao, Z.W. Yue, D. Yang, Z.H. Wang, Z.H. Li, H.H. Ge, Y.J. Li, *Corros. Sci.***53** (2011)1999–2005.
[3] D.Q. Zhang, L.X. Gao, G.D. Zhou, *Corros. Sci.***46**(2004) 3031–3040.
[4] N. Bellakhal, M. Dachraoui, *Mat. Chem. Phy.***85**(2004) 366–369.

[5] M. Dudukcu,G. Avcı, *Res. Chem.Intermed.***41**(2015)4861–4871.
[6] H. B. Ouici,M. Belkhouda, O. Benali , R. Salghi, L. Bammou, A. Zarrouk, B. Hammouti, *Res. Chem.Intermed.***41**(2015) 4617–4634.
[7] M. K. Pavithra , T. V. Venkatesha, M. K. Punith Kumar,K. Manjunatha, *Res. Chem.Intermed.***41**(2015) 7163–7177.
[8] A. Samide,B. Tutunaru, C. Negrilab,*Chem. Biochem. Eng. Quart.***3**(2011) 299–308.
[9] G. Gece, *Corros. Sci.***53** (2011) 3873–3898.
[10] I. Naqvi, A. R. Saleemi, S. Naveed, *Int. J. Electrochem. Sci*.**6**(2011) 146 –161 .
[11] I. Ahamad, R. Prasad, M.A. Quraishi, *Corros. Sci.***52**(2010) 3033–3041.
[12] I. Ahamad, R. Prasad, M.A. Quraishi, *J. Solid State Electrochem.***14** (2010) 2095–2105 .
[13] U. M. Eduok,M. Khaled, *Res. Chem.Intermed.***41**(2015) 6309–6324 .
[14] M. K. Pavithra, T. V. Venkatesha, M. K. Punith Kumar, N. S. Anantha, *Res. Chem.Intermed.* (2015)DOI 10.1007/s11164-015-2158-3 .
[15] S. Khorsand, K. Raeissi, F. Ashrafizadeh, *Appl. Surf. Sci.***305**(2014) 498–505 .
[16] N. Wang, D. Xiong, *Appl. Surf. Sci.***305**(2014) 603–608 .
[17] H. Dadafarin, E. Konkov , S. Omanovic, *Int. J. Electrochem. Sci*.**8**(2013)369–389 .
[18] P. Wang, D. Zhang , R. Qiu, Y. Wana, J. Wua, *Corros. Sci.***80**(2014) 366–373.
[19] M. K. Pavithra, T. V. Venkatesha, M. K. Punith Kumar, N. S. Anantha,*J. Electrochem. Sci. Eng.* ***5*(2)** (2015) 115-127.
[20] Y-C.Pan , Y.Wena, X-Y. Guo, P.Song , S. Shen , Y-P. Dub, H-F. Yang,*Corros. Sci.***73**(2013) 274–280.
[21] W.J. Guo, S.H. Chen, H.Y. Ma, *J. Serb. Chem. Soc.***71** (2006)167 –175.
[22] J. Zhang , X.L. Gong, H.H. Yu, M. Du, *Corros. Sci.***53** (2011) 3324–3330
[23] N. E. Hamdania, R. Fdila, M. Tourabi, C. Jama, F. Bentiss, *Appl. Surf. Sci.***357** (2015) 1294–1305 .
[24] M. Lebrini, F. Robert, C. Roos, *Int. J. Electrochem. Sci*.**6**(2011) 847–859.

J. Electrochem. Sci. Eng. **6(2)** (2016) 187-198; doi: **10.5599/jese.284**

Open Access : : ISSN 1847-9286

www.jESE-online.org

Original scientific paper

Etoricoxib selective sensor based on uracil-5,6-diamino-2-thio hydrochloride as neutral carrier for potentiometric analysis in pharmaceutical preparations

Salwa Fares Rassi✉

Department of Chemistry, Faculty of Science, Al-Baath University, Homs, Syria

✉Corresponding Author: rassi.salwa@gmail.com; Tel.: +963-966-243-153

Received: April 4, 2016; Revised: May 28, 2016; Accepted: May 29, 2016

Abstract

A construction and electrochemical behavior of novel potentiometric membrane sensor responsive to the etoricoxib was described. The sensor was based on the ion-pair complex of etoricoxib (ET) with uracil-5,6-diamino-2-thio hydrochloride (UDTH) (ET-UDTH) as exchange sites in a PVC matrix with different plasticizers dioctyl phthalate (DOPH) (electrode A), dibutyl phthalate (DBPH) (electrode B), and tri-n-butyl phosphate (TBP) (electrode C). The electrodes exhibited near-Nernstian response for ET-UDTH over the concentration range 0.051-40.042 mM. The electrode offered significant advantages including long lifetime (about 2 months), excellent stability and reproducibility, good response time (10-25 s), and wide pH working range (pH 5-12). Selectivity coefficients of ET related to a number of interfering cations and some organic compounds were investigated, and there were negligible interference caused by most of the investigated species. The direct determination of 0.5-10 mM of ET showed an average recovery of 99.03-101.75 % and a mean relative standard deviation 0.40-1.88. The results were obtained by determination of ET in tablets using the proposed electrodes which were comparable favorably with those obtained by spectrophotometric method.

Keywords

Etoricoxib, Uracil-5,6-diamino-2-thio hydrochloride, PVC membrane, Potentiometric method validation.

Introduction

Etoricoxib (5-chloro-6'-methyl-3-[4-(methylsulfonyl)phenyl]-2,3'-bipyridine) represents a second-generation of COX-2 inhibitors that has been developed for the treatment of many inflammatory diseases such as rheumatoid arthritis, osteoarthritis, pain relief and acute gout,

causing fewer gastrointestinal complications than conventional non-steroidal anti-inlammatory drugs (NSAIDs) [1-2]. The potential use of this COX-2 inhibitor among the general public is high due to their improved safety profile over traditional NSAIDs. Traditional NSAIDs such as aspirin and ibuprofen, inhibit both the COX-1 and COX-2 enzymes [3]. The COX-1 enzyme, which is expressed in essentially all tissues, has been found to play a role in the homeostasis of the gastrointestinal tract and kidneys, while the COX-2 enzyme is absent unless induced by an inflammatory event. Consequently, side effects of chronic use of traditional NSAIDs include gastrointestinal ulceration and bleeding [4]. Etoricoxib, a highly selective COX-2 inhibitor, was developed in order to address the safety issues associated with traditional NSAIDs, while providing pain relief from inflammatory illness such as osteo- and rheumatoid arthritis [5].

In order to provide quality control over the manufacture of any active pharmaceutical ingredient, it is essential to develop highly selective analytical techniques. Therapeutic importance of etoricoxib has prompted the development of many methods for its assay. The drug is available in tablet dosage form and is not yet official in any of the pharmacopoeias. Several methods have been reported for the analysis of etoricoxib in pharmaceutical dosage form as well as in the biological fluids and tissues, such as spectrophotometric methods [6-8], chromatographic methods HPLC [9-12], high-performance thin-layer chromatography [13], LC/MS spectrophotometry [14-18] and RP-HPLC method [6,19,20] for the estimation of etoricoxib.

Experimental

1. Reagents

All reagents used were of analytically pure grade and doubly distilled water was used throughout. High-molecular-weight poly(vinyl chloride) (PVC) was obtained from SABIC. Co., dioctyl phthalate 98.9 % (DOPH), tri-n-butyl phosphate 97 % (TBP), and di-n-butyl phthalate 99 % (DBPH) were obtained from BDH. Co., England. Tetrahydrofuran (THF) was obtained from Merck. Pure-grade etoricoxib (99.95 %) ($C_{18}H_{15}$ Cl N_2O_2S, 358.1 g mole^{-1}) was obtained from Aarti Drugs Limited (Indian). Uracil-5,6-diamino-2-thio hydrochloride (UDTH) ($C_4H_7N_4OSCl$, 194.5 g mole^{-1}) was synthesized (Figure 1) and identified in laboratory by spectroscopic means. The H-NMR and IR data (Figure 2) of UDTH are shown in Table 1.

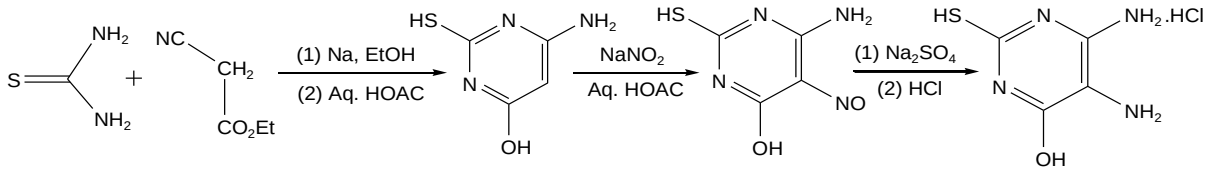

***Figure 1**. Synthesis of UDTH.*

2. Apparatus

Potentiometric and pH measurements was carried out using a digital Shott Gerate pH meter (Consort C 830, Belgium) with combined glass pH electrode. A water bath shaker (Grant instruments, Cambridge Ltd, England) was used to control the temperature of the test solutions. A saturated calomel electrode (SCE) was used as the external reference (Mettler, Switzerland) while an Ag/AgCl electrode was used as an internal reference. The electrochemical system may be represented as follows:

Ag/AgCl | inner solution | PVC membrane | test solution || KCl salt bridge || Hg/$HgCl_2$(sat.).

FT-IR 4100 (Fourier Transform Infrared Spectrometer) Jasco using KBr disk in the range 4000 - 400 cm^{-1}, Nernst glower, deuterium try glycine sulfate (DTGS), 0.1 cm^{-1}.

3. Preparation of solutions

Standard ET solutions (0.05-35 mM) were prepared in doubly distilled water. UDTH solution (10 mM) was prepared by dissolving appropriate amount of the compound in the methanol. ET and UDTH stock solutions were stored in dark bottle at refrigerator. Stock solutions of 1 M for each of LiCl, NaCl, KCl, NH_4Cl, $CaCl_2$, $MgCl_2$, $BaCl_2$, $ZnCl_2$, $MnSO_4$, $Ni(NO_3)_2$, $Co(NO_3)_2$, $Cu(NO_3)_2$, $Pb(NO_3)_2$, $FeCl_3$, $AlCl_3$, $CrCl_3$, glucose, fructose, lactose, starch, micro crystalline cellulose, carboxymethyl cellulose, polyethylene glycol, titanium dioxide, and polysorbate-80 were prepared by dissolving the appropriate amount of the compounds, and the diluted solutions from these were prepared by subsequent dilutions of the stock solutions.

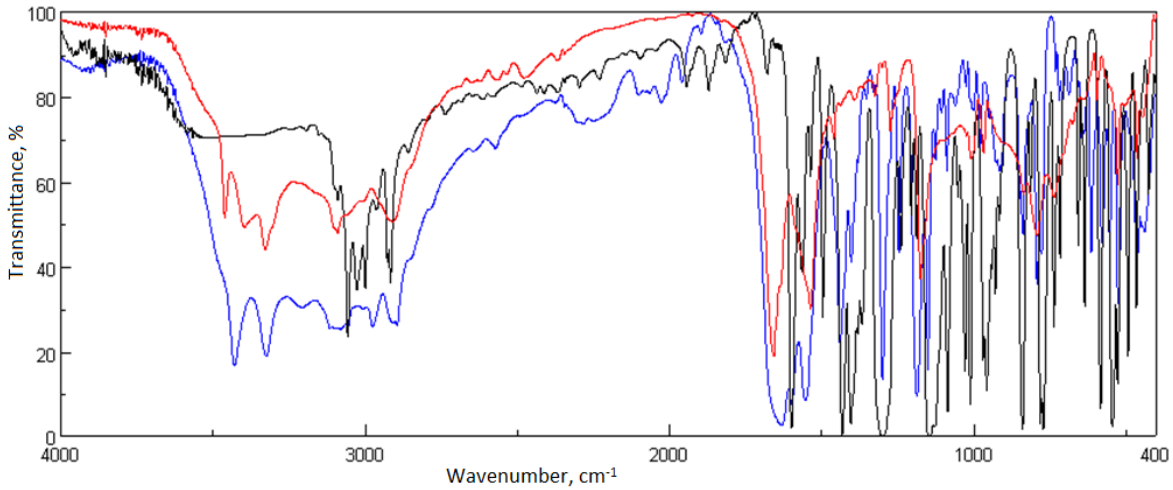

***Figure 2**. IR spectrum of etoricoxib (black spectrum), UDTH (red spectrum), and ET+UDTH- complex (blue spectrum)*

4. Sample Preparation

Etoricoxib tablets were supplied by Razi Pharmaceutical Industries (Aleppo, Syria). Each tablet was labeled to contain etoricoxib 120, 90, 60 mg/tab. The homogenized powder was prepared from ten accurately weighed ET tablets. An appropriate amount of this powder was dissolved in methanol and doubly distilled water. The mixture was then filtered and made up to the mark in a 100 mL volumetric flask. Different volumes of the stock solution were taken and subjected to the direct and standard addition methods.

5. Preparation of ion-pair compound

Ion-pair (ET^+UDTH^-) was prepared by mixing equal volumes of 10^{-2} M methanolic solution of ET with methanolic solution of UDTH with stirring. Methanol was then gradually evaporated to obtain a precipitate. ^{1}H-NMR and IR data (Figure 2) of ET^+UDTH^- are shown in Table 1.

6. Construction of etoricoxib membrane electrodes

The electrodes were constructed according to the method described by Craggs *et al.* [8]. Membrane composition was studied by varying the percentages (w/w) of the ion-pair complex, PVC and DOPH (electrode A), DBPH (electrode B), or TBP (electrode C) as plasticizing solvent mediators. The optimum composition that exhibited perfect performance characteristics was

reached. The membranes were prepared by dissolving the required amounts of ion pair complex, PVC and DOPH, DBPH or TBP in THF, and then the homogeneous mixture was poured into glass Petri dishes (8 cm diameter), covered with a glass plate, and allowed to evaporate overnight at room temperature. The thickness of obtained membrane was about 0.15 mm. Membranes (12 mm diameter) were cut out and then adhered to the polished end of a plastic cap attached to a glass tube using PVC-THF paste. The electrodes bodies were filled with a 1×10^{-1} M KCl solution and 1×10^{-3} M ET as the inner electrolyte, and then Ag/AgCl was inserted in it as internal reference electrode. Electrode potential was measured against the SCE as the reference electrode. Before use, the electrode membranes were conditioned by immersion in 25 mM of ET solution for 3 h.

***Table 1**. H-NMR and IR data for UDTH and Complex between UDTH and ET.*

	δ / ppm			Wavenumber, cm^{-1}	
	ET^+UDTH^-	UDTH		UDTH	ET^+UDTH^-
-SH	---	12.48	-SH	2479	---
-OH	11.53	11.55	-OH	3460	3440
$-NH_3^+$	4.28	6.27	$-NH_2$	3328-3390	3250-3325
$-NH_2$	7.74	8.00	N-S	---	1186
$-CH_3$	2.76				
$-CH_3$	3.25				
9 H aromatic	7.88-8.57				

7 Selectivity of sensors

Potentiometric selectivity coefficient, $K^{pot}_{A,B}$, of an ion-selective electrode (ISE) was commonly used as quantitative expression of the ability of the electrode to respond primarily to the analyte in the presence of interfering ions. The effect of the presence of some different species on the response of ET electrodes was investigated, and the selectivity coefficient $K^{pot}_{A,B}$ of the proposed electrodes was calculated in the presence of related organic and inorganic substances using matched potential method (MPM) [9-10]. The selectivity coefficient, $K^{pot}_{A,B}$, which was measured by matched potential method was calculated according to the following equation:

$$K^{MPM}_{A,B} = \frac{(a'_A - a_A)}{a_B} \quad (1)$$

where a'_A is the known activity of primary ion, a_A is the fixed activity of primary ion, and a_B is the activity of interfering ions.

8. General procedures

The performance of the three electrodes prepared was investigated by measuring e.m.f. values of 0.05-45 mM of ET. The electrodes were calibrated by added volumes of 50 mM stock solution of ET successively in 50 ml of water to generate a total concentration ranging from 0.05 to 45 mM ET, followed by immersing the ET-electrode, together with a SCE in the solution. The potential reading was recorded after stabilization, and the e.m.f was plotted as a function of the logarithm of the ET concentration. The concentration graph was used for subsequent determinations of unknown ET concentrations. The e.m.f. measurements with the polymeric membrane electrodes were carried out with the cell assembly shown schematically in the section 2.2.

9. Potentiometric determination of ET

ET was determined potentionmetrically by the direct and standard addition methods [11-12]. In this method the proposed electrodes (A,B) (ET-UDTH) were immersed into a sample of 15 ml with an unknown concentration of a ET solution, and the equilibrium potential, E_u, was recorded. Then 1 ml of 50 mM of standard ET was added into the testing solution and the equilibrium potential, E_s, was obtained. From the potential change, $\Delta E = E_u - E_s$, we could determine the concentration of the testing sample using the equation:

$$C_x = \frac{C_s V_s}{(V_x + V_s) \times 10^{\Delta E/S} - V_x} \quad (2)$$

where C_x and V_x are concentration and volume of an unknown sample, C_s and V_s are concentration and volume of the standard, respectively. S is the slope of the calibration graph (slope of the electrode response), and ΔE is the difference in (mV) between e.m.f. after and before addition of the standard solution. Standard addition method was applied for determining ET in commercial preparations.

Results and discussion

1. Optimization of the membrane composition

The effect of the amount of ion pair in the membrane phase on the potentiometric response was investigated. The data shown in Table 2 clearly indicate that the electrode (V) with 5 wt% of ET-UDTH ion pair has performance characteristics (slope 57.00 mV decade^{-1}, at 25 °C, usable concentration range, 0.031-40.042 mM ET), and response time 25 s. For all construted electrodes, the percentage of ion-pair ranging from 1 to 8 % was found to offer better slopes and correlation coefficients. The results obtained with ion-pair for the three plasticizers are summarized in Table 2. The electrodes A and B exhibit comparable linear ranges and the lowest detection limit.

Table 2. *Optimization of the membrane ingredients.*

Composition, % (w/w)				Slope, mV decade-^{1}	Detection limit, mM
Membrane	**Ion-pair Complex**	**PVC**	**DBPH**		
I	1	49.5	49.5	48.62	0.39
II	2	49.0	49.0	50.24	0.31
III	3	48.5	48.5	53.14	0.25
IV	4	48.0	48.0	55.69	0.19
V	**5**	**47.5**	**47.5**	**57.00**	**0.13**
VI	6	47.0	47.0	54.06	0.25
VII	7	46.5	46.5	52.09	0.20
VIII	8	46.0	46.0	49.51	0.34

2. Effect of the internal filling solution

The concentration of the internal solution of ET in the electrode was changed from 10 to 0.01 mM and the potential response of the electrode was measured. It was found that variation of the concentration of the internal solution did not cause any significant difference in the potential response of the electrode. ET concentration of 1 mM as internal solution was quite appropriate for proper functioning of the electrode.

3. Effect of plasticizer type on the characteristic performance of the sensor

Three plasticizers, DOPH, DBPH and TBP were evaluated. As shown in Table 3, the best performances, in terms of slopes, linear range and detection limit obtained had the following order: DBP (electrode B) > DOPH (electrode A) > TBPH (electrode C). The working characteristics for the electrodes were assessed on the basis of their calibration curves. The TBP which had a low viscosity (3.11 cSt), led to leaching of the complex from the membrane. All further studies were conducted using DBPH and DOPH as plasticizers.

Table 3. *Effect of the nature of an ion-pair and a plasticizer on characteristics of the electrodes.*

Electrode	**A**	**B**	**C**
Ion-pair complex, wt %	5	5	7
Plasticizer	DOPH	DBPH	TBP
Slope, mV decade^{-1}	56.26	57.00	41.23
Linear range, mM	0.051-39.810	0.031-40.042	0.653-33.140
Correlation coefficient	0.9997	0.9999	0.9699
Detection limit, mM	0.042	0.023	0.324

4. Effect of soaking

Freshly prepared electrodes must be soaked to activate the surface of the membrane to form an infinitesimally thin layer for ion-exchange process to occur [13]. This preconditioning process required different times, depending on the diffusion of ions and their equilibrium at the electrode test solution interface. Fast establishment of equilibrium was certainly a condition for a fast potential response. Thus, the performance characteristic of the ET electrode was investigated as a function of the soaking time. For this purpose the electrode was soaked in a 50 mM solution of ET, UDTH and water at room temperature. The optimum soaking time and the optimum solution was found to be 3 h for 50 mM solution of ET. During this period sensors were washed with water after each application and kept dry in air at room temperature when off-use. The results indicate that for a time of 3 h of soaking the slope remained constant at about 57.00 mV decade^{-1}, at 25 °C. *E*, mV *vs. t*, min plots (Fig. 3) were obtained after the electrode was soaked continuously in 50 mM ET, water and UDTH for 30-630 min.

5. Effect of pH

The influence of the pH on the potentiometric responses of membrane electrodes was investigated by following the potential variation over the pH range of 1-14. The electrode response for different ET concentration was tested at various pH values. The pH of the solution was adjusted by adding small volumes of hydrochloric acid or sodium hydroxide to the test solution. As can be seen from Figure 4, membrane electrode exhibited a negligible potential change within the pH range of 5-12. At lower pHs (pH<6) there was a decrease in potential which may be due to the interference of hydronium ion and the penetration of H_3O^+ into the membrane surface, or a gradual increase of the protonated species [14-15].

6. Effect of the temperature of the test solution

The effect of the temperature of the test solution on the potential response of the membrane was tested by following the slopes variation in the temperature range 20-65 °C (Fig. 5). The results show that within the temperature range investigated the electrodes respond practically to the ET concentration with slopes from 54.23 to 57.30 mV decade^{-1} and usable concentration range of about 0.031-40.042 mM.

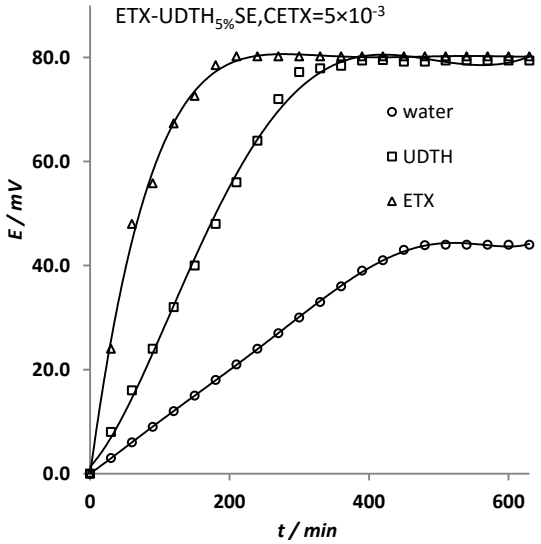

Figure 3. Effect of stock solution on response electrode

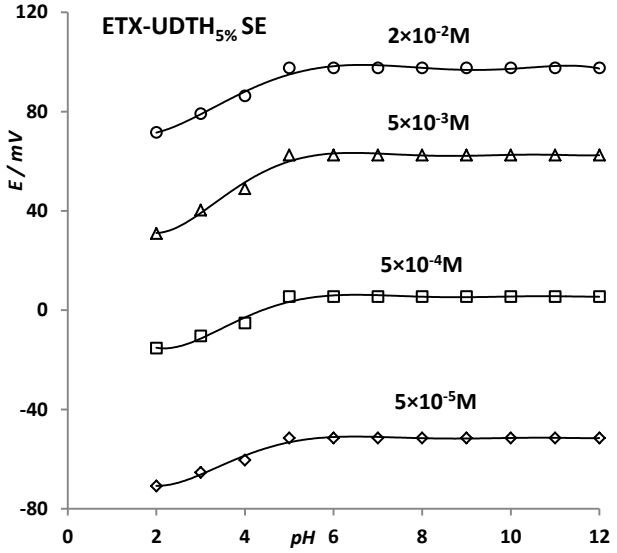

Figure 4. *Effect of the pH on the response of the electrode*

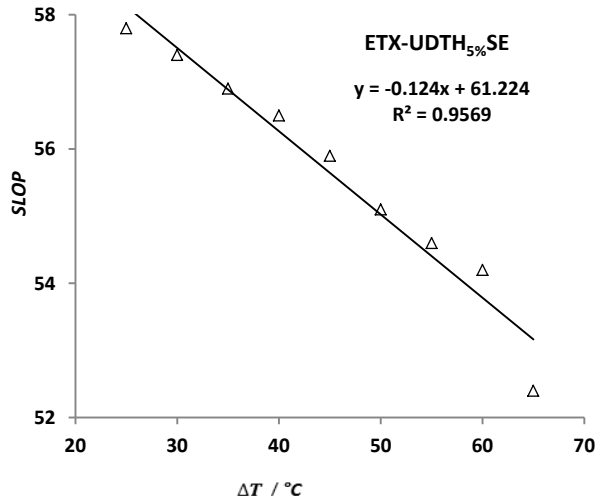

Figure 5. Effect of the temperature of the test solution on the potential response of the membrane.

7. Calibration graphs

Using the optimized membrane composition and conditions described above, the potentiometric response of the electrode was studied based on the ET concentration in the range of 0.01- 50 mM. The calibration curves for the electrodes A and B containing DOP or DBP as plasticizer gave an excellent linear response from 0.031 to 40.042 mM, as shown in Figure 6. The results given in Table 3 show the characteristics performance of the membrane electrodes. The least squares equation obtained from the calibration data was as follows:

E/ mV = S × log([ET,M]) + intercept

where E is the potential and S the slope of the electrodes.

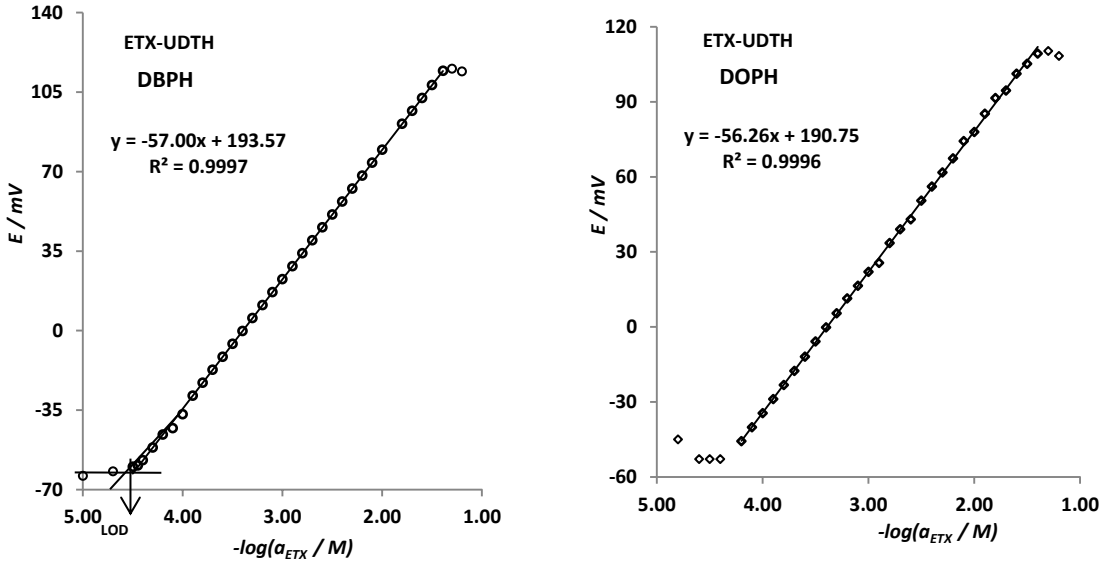

Figure 6. *Calibration graph of ET membrane electrode.*

Table 4. *Response characteristics of membrane electrodes*

Electrode number	A	B
Plasticizer	DOPH	DBPH
Parameter		
Slope, mV/decade^{-1}	56.26	57.00
Correlation cofficient	0.9996	0.9997
Linearity range, mM	0.051-39.810	0.031-40.042
Lower detection limit, mM	0.042	0.023
Response time, s	t ≤35	t ≤25
Working pH range	5.0-12.0	5.0-12.0
Temperature, °C	25	25
Life time, days	44	55

8. Response time

The time required for the electrodes to reach steady potential values, after immersing the electrode in different concentration namely from 0.05, 0.5, 5 and 25 mM of ET solution was studied. The average time was found to be short, ranging from 10 s for concentrations 25 mM and 5 mM, to about 25 s for 0.05 mM solution. Two electrodes gave the same range of response times. These values indicated the high stability of the electrodes during the measurements. A typical plot for response time is shown in Fig. 7 for the electrode based on DBP as the plasticizer.

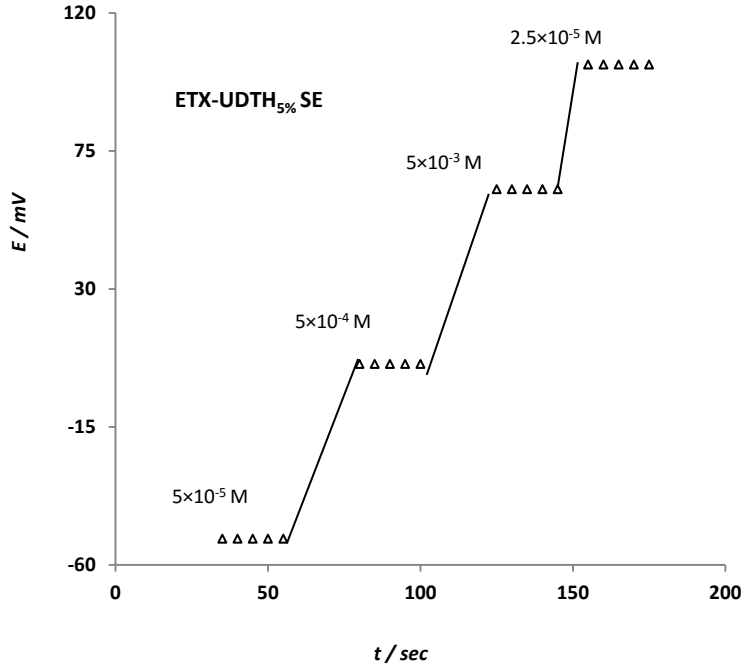

Figure 7. *Plot the response time of DBP electrode using 0.05, 0.5, 5, 25 mM etoricoxib.*

9. Lifetime

The electrode lifetime was investigated by performing the calibration curve and the periodic testing of standard solutions (0.031-40.042 mM of ET) and calculating the response slope. It was observed that the electrode B exhibited good stability in terms of slope in the linear domain of concentration and the electrodes could be used continuously for about 55 days without considerable decrease in its slope value. Electrode A exhibited good stability in terms of slopes of 56.20 to 53.4 mV decade^{-1} in the linear domain of concentration from 0.051 to 39.810 mM. This electrode could be used continuously for about 44 days. But two changes were observed, firstly, a slight gradual decrease in the slope (from 57.00 to 55.23 mV decade^{-1}) was found, and secondly an increase in the detection limit (from 0.023 to 0.2 mM) was noted. However, the electrode with DBP as plasticizers could be used for about 55 days without any considerable decrease in the slope value.

10. Selectivity of electrode

The influence of some inorganic cations such as of Li^+, Na^+, K^+, $Ca^{2+,}$ Zn^{2+}, Ba^{2+}, Mn^{2+}, Mg^{2+}, Ni^{2+}, NH_4^+, Cu^{2+} pb^{2+}, CO^{2+}, Fe^{3+}, Al^{3+}, Cr^{3+}, and some organic compound like sugars (glucose, fructose) and excipients on the electrode response was investigated. The selectivity of the electrode was measured by applying the matched potential method (MPM). According to this method, the activity of ET was increased from a_A = 1 mM (reference solution) to a'_A=1.1 mM, and the changes in potential (ΔE) corresponding to this increase were measured. Then a solution of an interfering ion of concentration a_B is added to a new 1 mM reference solution until the same potential change (ΔE) was recorded. The selectivity factor, $K_{A,B}^{pot}$, for each interference was calculated using equation (1). The results are given in Table 5. Results revealed reasonable selectivity for ET in presence of many related substances. The selectivity coefficient obtained by this method showed that there were no significant interferences from the cations, this reflected a very high selectivity of the investigated electrode towards ET.

Table 5. *Selectivity coefficients for of the ET-UDTH responsive electrode.*

$K^{MPM}_{A,B}$	**Interferent**	$K^{MPM}_{A,B}$	**Interferent**
9.9×10^{-5}	Glucose	1.00×10^{-4}	Li^{+1}
2.0×10^{-5}	Fructose	1.25×10^{-4}	K^{+1}
2.5×10^{-5}	Lactose	9.09×10^{-5}	Na^{+1}
4.3×10^{-5}	starch	5.56×10^{-5}	$NH4^{+}$
8.0×10^{-4}	Microcrestaline cellulose	6.25×10^{-5}	Mg^{+2}
1.2×10^{-5}	Carboxymetyle cellulose	6.45×10^{-5}	Mn^{+2}
6.2×10^{-6}	polyethylene glycol	1.10×10^{-5}	Ca^{+2}
4.8×10^{-5}	titanium dioxide	7.14×10^{-5}	Ba^{+2}
8.6×10^{-6}	polysorbate 80	5.13×10^{-5}	Ni^{+2}
		5.81×10^{-5}	Cu^{+2}
		7.69×10^{-5}	Zn^{+2}
		9.52×10^{-5}	pb^{+2}
		7.81×10^{-5}	Cd^{+2}
		6.76×10^{-5}	Cr^{+3}
		1.22×10^{-5}	Fe^{+3}

Even though, the inorganic cations have different ionic sizes, mobilities and permeabilities they did not interfere with ET. The selectivity of the electrode towards neutral sugars was evaluated. The tolerance was considered as the concentration imparting a ± 0.2 mV drift in the potential reading. The results indicated that glucose, fructose, lactose and starch did not interfere. The experiments showed no interference with respect to ET response for electrodes A and B.

11. Analytical application

The ET membrane electrodes were used for the determination of ET in pharmaceutical preparations using both direct and standard-addition methods. The direct method is the simplest for obtaining quantitative results. A calibration graph was constructed and concentration of the unknown was calculated from the linear equation of the calibration curve. Direct determination of ET in tablets was carried out using the developed membrane electrodes. The results are summarized in Table 6 and 7.

Table 6. *Accuracy and precision for the determination of ET using the proposed PVC membrane sensors in pure solution*

		Direct mothed				**Standard-addition method**			
Electrode	**Taken, mM**	**Found, mM**	**RSD, %**	***R* / %**	**ASE**	**Found, mM**	**RSD, %**	***R* / %**	**ASE**
A	0.5	0.50	1.88	100.00	0.005	0.49	2.13	98.00	0.007
	2.5	2.49	1.80	99.60	0.026	2.44	1.97	97.60	0.034
	5	4.95	1.45	99.00	0.042	5.08	1.74	101.60	0.063
	10	9.95	0.86	99.50	0.050	9.94	1.56	99.40	0.110
B	0.5	0.49	1.52	98.00	0.004	0.51	1.46	102.00	0.005
	2.5	2.54	1.24	101.70	0.018	2.53	1.32	101.20	0.024
	5	4.98	0.81	99.60	0.023	4.98	1.01	99.60	0.036
	10	10.06	0.62	100.60	0.035	10.19	0.91	101.90	0.068

Average of four determinations

The content of drug in its formulation had good agreement with the declared amount. The standard-addition method was applied by adding a small portion (1 mL) of a 50 mM standard ET solution to 15 mL of various formulation drug concentrations (60, 90, 120) mg ET/tablet, (0.167,

0.251, 0.335) mM. The change in the potential reading (at a constant temperature of 25 °C) was recorded after each addition, and was used to calculate the concentration of ET by the equation (2). Thus, the determination of the concentration depended mainly on Δ*E*, hence, to obtain a noticeable Δ*E* we needed to prepare a higher concentration of the ET standard. Results of the standard-addition method are given in Table 7.

The determination of ET in tablet was carried out using the proposed electrode. The results were compared to those obtained using the spectrophotometric method [16]. The determination of ET in its pharmaceutical formulations Etoxia gave an average Recovery of (100.06-100.75). Mean values were obtained with a Student's t- and F-tests at 95 % confidence limits for four degrees of freedom are shown in Table 7. The data reveal that results compare favorably with those obtained by spectrophotometric. The results showed comparable accuracy (*t*-test) and precision (*F*-test).

Table 7. *Determination of ET in its pharmaceutical preparation using the proposed electrode.*

Sample	Nominal value	Potentiometry		Spectrophotometry
	mgET/tablet	Direct	Standard addition	
Etoxia	60			
***R* / %±SD**[a]		100.75±0.58	100.47±0.61	99.73±0.31
***t*-Value**[b]		1.85	1.72	1.830
***F*-Value**[b]		3.50	3.87	
Etoxia	90			
***R* / %±SD**[a]		100.29±0.49	100.43±0.54	100.08±0.33
***t*-Value**[b]		1.32	2.15	0.57
***F*-Value**[b]		2.20	1.86	
Etoxia	120			
***R* / %±SD**[a]		100.06±0.23	100.46±0.55	100.46±0.49
***t*-Value**[b]		1.89	0.58	2.05
***F*-Value**[b]		1.26	4.53	

a Five independent analyses.

b Theoretical values for t- and F-values at four degree of freedom and 95% confidence limit are (t=2.776) and (F=6.26).

Conclusions

In conclusion, the developed PVC membrane sensors described in this work offer a simple, accurate, selective, and specific tool for quantitative determination of ET in some pharmaceutical formulations. The membrane sensor ET-UDTH based on DBPH, seem to be better than ET-UDTH based on DOPH with respect to calibration, slop, and accuracy. The statistical evaluations of the proposed method in comparison with spectrophotometric method indicate that the method is accurate and precise. The proposed analytical method is proved to be simple and rapid, with good accuracy**.**

References

[1] D. Riendeau., M.D. Percival, C. Brideau, S. Charleson, D. Dube, D. Ethier, J.-P. Falgueyret, , R.W. Friesen, R. Gordon, G. Greig, J. Guay, J. Mancini, M. Ouellet, E. Wong, L. Xu, S. Boyce, D. Visco, Y. Girard, P. Prasit, R. Zamboni, I.W. Rodger, M. Gresser, A.W. Ford-Hutchinson, R.N. Young, C.-C. Chan, *J. Pharmacol. Exp. Ther.* **296(2**) (2001) 558-566.

[2] A.D. Rodrigues, R.A. Halpin, L.A. Geer, D. Cui, E.J. Woolf, C.Z. Matthews, K.M. Gottesdiener, P.J. Larson, K.C. Lasseter, N.G.B. Agrawal, *Drug Metab. Dispos.* **31 (2)** (2003) 224-232.

[3] B. Cryer, M. Feldman, *Am. J. Med.* **104** (1998) 413-421.

[4] M.C. Allison, A.G. Howatson, C.J. Torrance, F.D. Lee, R.I. Russell, *New Engl. J. Med.* **327** (1992) 749-754.
[5] R.W. Friesen, C. Brideau, C. Chan, S. Charleson, D. Deschenes, D. Dube, D. Ethier, R. Fortin, J. Gauthier, Y. Girard, R. Gordon, G.M. Greig, D. Reindeau, C. Savoje, Z. Wang, E. Wong, D. Visco, J. Xu, R.N. Young, *Bioorg. Med. Lett.* **8** (1998) 2777-2782.
[6] R.M. Singh, Y. Kumar, D.K. Sharma, S.C. Mathur, G.N. Singh, T.A. Ansari, S. Jamil, *Indian. Drugs* **42(8)** (2005) 535-536.
[7] B.N. Suhagia, H.M. Patel, S.A. Shah, I.S. Rathod, B.P. Marolia, *Indian J. Pharm. Sci.* **67(5)** (2005) 634-637.
[8] A. Craggs, G.J. Moody, J.D.R. Thomas, *J. Chem .Edu.* **51** (1974) 541-544.
[9] Y. Umezawa, K. Umezawa, H. Sato, *Pure. Appl. Chem.* **67(3)** (1995) 507-518.
[10] Y. Umezawa, Ph.B. Hlmann, K. Umezawa, K. Tohda, Sh. Amemiya, *Pure. Appl. Chem.* **72** (2000) 1851-2082.
[11] E. Baumann, *Anal. Chem. Acta* **42** (1968) 127-132.
[12] S. TNVSS, D Aditya, T. Santosh, B. S. Sundar, IAJPR **3(4)(**2013) 3044-3056.
[13] D. G. Peters, J. M. Hayes, G. M. Hieftje, *Chemical Separations and Measurements.* W.B. Saunders, Philadelphia, 1974, pp 835.
[14] Y. M. Issa, M. M. Hassouna, F. M. Abdel-Gawad, E. M. Hussien, *J. Pharm. Biomed. Anal.* **23(2-3**) (2000) 493-502.
[15] R. I. Stefan, H. Y. Aboul-Enein, G. E. Baiulescu, *Sens. Actuators B* **37** (1996) 141-144.
[16] M. Arvand, M. Vejdani, M. Moghimi, *Desalination* **225** (2008) 176-184.
[17] K. Shah, A. Gupta, P. Mishra, *J. Chem* **6(1***)* (2009) 207-212.
[18] P.G. Sunitha, N. Deattu, R. Ravi Kumar, S. Sri Rudhra, P. Kalaimathi, B. Soundiramani, A.C.M.S **(1)** (2015) 36-38.
[19] R. Chandra, A. Sanghi, D. Kumar, K.K. Hindwan, *British Biomedical Bulletin* **2 (4)** (2014) 706-714.
[20] S. Gholve, O. Bhusnure, O. Mathew1and J. Sangshet, *Int. J. Pharm. Bio. Sci.* **7(2)** (2016) 246–253.

J. Electrochem. Sci. Eng. **6(2)** (2016) 199-213; doi: **10.5599/jese.290**

Open Access : : ISSN 1847-9286

www.jESE-online.org

Original scientific paper

Electrocoagulation removal of anthraquinone dye Alizarin Red S from aqueous solution using aluminum electrodes: kinetics, isothermal and thermodynamics studies

Abideen Idowu Adeogun*,**,✉, Ramesh Babu Balakrishnan**

**Department of Chemistry, Federal University of Agriculture, Abeokuta, Nigeria*
***Electrochemical Pollution Control Division, CSIR - Central Electrochemical Research Institute. Karaikudi 630006, India*

✉Corresponding Author: abuaisha2k3@yahoo.com, Tel: +23480306126987 and +918098772434

Received: May 3, 2016; Revised: May 22, 2016; Accepted: May 23, 2016

Abstract

Electrocoagulation (EC) was used for the removal of anthraquinone dye, Alizarin Red S (ARS) from aqueous solution. The process was carried out in a batch electrochemical cell with Al electrodes in a monopolar connection. The effects of some important parameters such as current density, pH, temperature and initial dye concentration, on the process were investigated. Equilibrium was attained after 10 minutes at 30 °C. Pseudo-first order, pseudo-second order, Elovic, and Avrami kinetic models were used to test the experimental data in order to elucidate the kinetics of the electrocoagulation process; pseudo-first order and Avrami models best fitted the data. Experimental data were analyzed using six isotherm models: Langmuir, Freudlinch, Redlich–Peterson, Temkin, Dubinin–Radushkevich and Sips isotherms and it was found that the data fitted well with Dubinin–Radushkevich and Sips isotherm model. The study showed that the process depended on the current density, temperature, pH and initial dye concentration. The calculated thermodynamics parameters (ΔG^o, ΔH^o and ΔS^o) indicated that the process is spontaneous and endothermic in nature.

Keywords

Batch; Electrochemical cell; Mnopolar connection; Pseudo first order; Equilibrium; Spontaneous.

Introduction

The advanced in technologies for industrialization and urbanization has substantially enhanced the degradation of the environment especially the aquatic environment, through the discharge of industrial wastewaters and domestic wastes [1,2]. The residual dyes from different sources such

as: textile, paper and pulp, dye and dye intermediates, pharmaceutical, tannery, and kraft bleaching industries are considered as organic coloured pollutants [3–6]. These industries utilize large quantities of a number of dyes with residues leading to the large amount of coloured wastewaters, toxic and even carcinogenic, posing serious hazard to aquatic living organisms. Most dyes used in industries are stable to light, heat and oxidation, they are not biologically degradable and are also resistant to aerobic digestion and even when they does, they produce toxic and hazardous products [7,8].

Anthraquinone dye Alizarin Red S (ARS) is available as sodium salt of 1,2-dihydroxy-9,10-anthraquinonesulfonic acid (Fig. 1) and it is referred to as Mordant Red 3, C.I. no. 58005. Alizarin, a natural dye obtained from madder (*Rubiatinctorum, L. Rubiaceae*) by sulphonation, is a water-soluble and widely used anthraquinone dye in textile and as a stain in clinical study of synovial fluid to assess basic calcium phosphate crystals [9]. ARS is a durable pollutant when released to aquatic ecosystems. It cannot be completely degraded by general physicochemical and biological processes because of the complex structures of the aromatic rings that afford high physico-chemical, thermal, and optical stability [7,10]. Therefore, most treatments for such dye-laden effluents are largely inadequate; however, removal of this dye from industrial wastewaters is a crucial process, from both economic and environmental points of view [11].

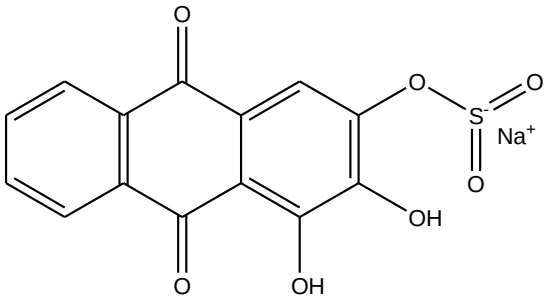

Figure 1. *Structure of Alizarin Red S (ARS)*

Electrochemical techniques which include electrooxidation, electrochemical reduction, electro-coagulation, electroflotation [12], have been developed for the treatment of organic pollutants in waste water with higher efficiency than any other biological, physical and chemical process [13,15]. Electrocoagulation has been known for some time as a process capable of fractionating a number of organic substances in a rather efficient manner. The coagulants are generated in-situ by electrooxidation of the anode. The mostly used anode materials are iron and aluminum because of their availability and relatively low cost. Electrocoagulation is accomplished in a three step processes as follows: (i) electrolytic reactions at surface of electrodes, (ii) formation of coagulants in aqueous phase and (iii) adsorption of soluble or colloidal pollutants onto coagulants and removal of them using sedimentation or flotation of flocs when hydrogen gas bubbles were produced at the cathode [16].

Several methods have been used for the removal of ARS from wastewaters, these include adsorption [17-19], electrochemical degradation [20-23] and electro-Fenton process [24] using various electrodes. However, to the best of our knowledge, kinetics and isothermal studies have not been elucidated in any of these studies.

In this study, ARS was removed from aqueous solution in a mono-polar electrochemical cell using aluminum electrodes. The effect of current density, initial dye concentration, electrolyte concentration, pH and temperature were studied. Adsorption kinetics of electrocoagulants was analyzed with pseudo-first order, pseudo-second order, Elovic, and Avrami kinetic models. The

diffusion mechanism was analyzed with intraparticulate diffusion model while the equilibrium adsorption behaviour was analyzed by fitting the equilibrium data with six isotherm models. Thermodynamic parameters such as free energy (ΔG), enthalpy (ΔH) and entropy (ΔS) were also determined to understand the spontaneity of the electrocoagulation process.

The following reactions were envisaged at the electrodes:

Anodic reaction:

$$Al \rightarrow Al^{3+} + 2e^{-} \quad (1)$$

Cathodic reaction:

$$3H_2O + 3e^{-} \rightarrow 3OH\text{-} + 3/2H_2\ 3H_2O \quad (2)$$

Overall reaction:

$$Al^{3+} + 3OH^{-} \rightarrow Al(OH)_3 \quad (3)$$

Experimental

Dye solution preparation

Alizarin Red S (sodium alizarin sulphonate (Fig. 1), CI 58005, Product No. – 13005) was a product of British Drug House, Poole, England. 1000 mg L^{-1} aqueous solution of ARS was prepared with de-ionized water as the stock solution and was further diluted with de-ionized water to obtain the working standard solutions. The pH of the solution was adjusted when necessary with aliquots of 1.0 mol L^{-1} of HCl and NaOH before the commencement of the experiment. The conductivity of the solution was maintained with NaCl solution as the electrolyte.

Experimental apparatus and procedures

Figure 2 depicts the electrocoagulation cell which consists of a 0.6 L glass cell fitted with a polycarbonate cell cover with slots to introduce the electrodes, thermometer and electrolyte. The aluminum electrodes of dimensions 4.5×7×0.3 cm with inter electrode distance of 2 cm were fully immersed in the 0.5 L solution of the dye. A regulated direct current (DC) was supplied from a rectifier (0 – 2 A, 0 – 35 V; Applab 7711 multi-output). The temperature of the electrolyte was controlled to the desired value with a variation of ±1 °C by adjusting the temperature knob on the IKA RCT Basic magnetic hotplate stirrer and was allowed to equilibritate before the commencement of the experiment.

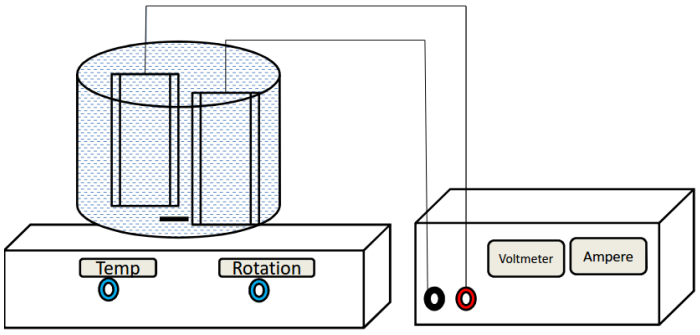

Figure 2. *Laboratory scale electrocoagulation cell*

Analytical procedure

The concentration of the dye in solution was estimated using spectrophotometer (UV-VIS –NIR VARIAN 500 Scan CARY). To compare the dye obtained from the coagulation with the original ARS

dye, the flock is filtered and the residue dried at 105 °C for 30 minutes, then the FTIR of the two samples (ARS and residue) were obtained using FTIR spectrophotometer (TENSOR 27 Bruker Optik GmbH, Germany). Non-linear regression analysis method using a program written on Micro Math Scientist software (Salt Lake City, Utah) was used to obtain the least square fit for all the models.

Equilibrium studies

The effects of current density, initial dye concentration, electrolyte concentration, pH and temperature on the electrocoagulation removal of ARS were studied. Sample solutions were withdrawn at intervals to determine the residual dye concentration by using UV-VIS-NIR spectrophotometer. The amount of dye coagulated at equilibrium, Q_e / mg g^{-1}, was calculated using equation 4 below:

$$Q_e = \frac{(C_o - C_e)V}{W} \quad (4)$$

where C_o / mg L^{-1} is the initial concentration and C_e /mg L^{-1} is the concentration of the dye at equilibrium in the liquid-phase. V is the volume of the solution, L while W is the mass of the coagulant which can be estimated from Faraday Law according to the equation 5:

$$W = \frac{MIt}{nF} \quad (5)$$

M is the molar mass (g mol^{-1}) of the elements, I is the current (A), t is the electrocoagulation time in seconds, n is the number of electrons involved and F is Faraday's constant (96,485 C mol^{-1}).

The percentage dye removal as colour was estimated by:

$$\text{Colour removal}, \% = \frac{(Abs_0 - Abs_e)}{Abs_0} \times 100 \quad (6)$$

where $Abs_{0,}$ is the blank absorbance and Abs_e is the absorbance at equilibrium.

Adsorption isotherms

The equilibrium data from this study were described with the six adsorption isotherm models. These are models by Langmuir [25], Freudlinch [26], Temkin [27], Dubinin and Radushkevich [28], Sip [29] and Redlich and Peterson [30]. The acceptability and suitability of the isotherm equation to the equilibrium data were based on the values of the correlation coefficients, R^2 estimated from linear regression of the least square fit statistic on Micro Math Scientist software.

Electrocoagulation kinetics studies

Since the amount of coagulant can be estimated for a given time, the pollutant removal can be modelled using an adsorption phenomenon. The procedures for the kinetics studies were basically identical to those of equilibrium tests. The aqueous samples were taken at preset time intervals, and the concentrations of the dye were similarly determined. The amount of dye removed at time t, Q_t (mg g^{-1}), was calculated using Equation 7:

$$Q_t = \frac{(C_o - C_t)V}{W} \quad (7)$$

where C_o / mg L^{-1} is the initial concentration and C_t / mg L^{-1} is the concentration of the dye at time t in the liquid-phase. V is the volume of the solution (L), and W is the mass of $Al(OH)_3$ calculated as stated in eqn. 5 above. In order to investigate the mechanisms of the adsorption process, pseudo-

first order, pseudo-second order, Avrami, and Elovich models respectively were applied to describe the kinetics of adsorption of ARS to $Al(OH)_3$ generated during the electrocoagulation process. Since the diffusion mechanism cannot be obtained from the kinetic model, the intra-particulate diffusion model [8] was also tested. A model is adjudged best-fit and selected based on statistical parameters.

Statistical test for the kinetics data

The acceptability and hence the best fit of the kinetic data were based on the square of the correlation coefficients R^2 and the percentage error function which measures the differences (SSE, %) in the amount of the dye concentration coagulated at equilibrium predicted by the models, (Q_{cal}) and the actual, (*i.e.* Q_{exp}) measured experimentally. The validity of each model was determined by the sum of error squares (SSE, %) given by:

$$\text{SSE, \%} = \sqrt{\frac{((Q_{exp} - Q_{cal})/Q_{exp})^2}{N-1}} \times 100 \quad (8)$$

N is the number of data points. The higher is the value of R^2 and the lower the value of SSE; the better fitted the data.

Thermodynamics of electrocoagulation process

Arrhenius equation is applied to estimate the activation energy of adsorption according to the relationship:

$$\ln k = \ln A - \frac{E_a}{RT} \quad (9)$$

where k is the rate constant obtained from the kinetic model, E_a is the Arrhenius activation energy of adsorption, (kJ/mol), A is the Arrhenius factor, R is the universal gas constant (8.314 J mol^{-1} K^{-1}) and T is the absolute temperature. The thermodynamics parameters i.e. ΔG°, ΔH° and ΔS° were estimated using the following relation:

$$\Delta G^\circ = -RT \ln K_d \quad (10)$$

$$\ln K_d = \frac{\Delta S^\circ}{R} - \frac{\Delta H^\circ}{RT} \quad (11)$$

The equilibrium constant, $K_{d,}$ is obtained from the value of Q_e/C_e at different temperature equilibrium study. Van't Hoff plot of ln K_d against the reciprocal of temperature (1/T), should give a straight line with intercept as $\Delta S_o/R$ and slope as $\Delta H_o/R$.

Results and discussion

Batch equilibrium studies

Effect of current density

The amount of coagulants generated is related to the time and current density [31]. Current density determines the coagulant production rate, and adjusts the rate and size of the bubble production, and hence affects the growth of flocs [32,33]. The effect current density on the removal of ARS, were carried at the current density varied between j of 7.15 to 35.77 A m^{-2}. Figure 3 shows the plot of current density versus the percentage colour removal by the

electrocoagulation process. From the figure it is glaring that as the current density is increased the rate of colour removal also increased from 96 to 99.31 %. Increasing current density results in a corresponding increase in the production of coagulant in the solution leading to high efficiency. The optimum current density of 35.77 A m^{-2} was used throughout the study.

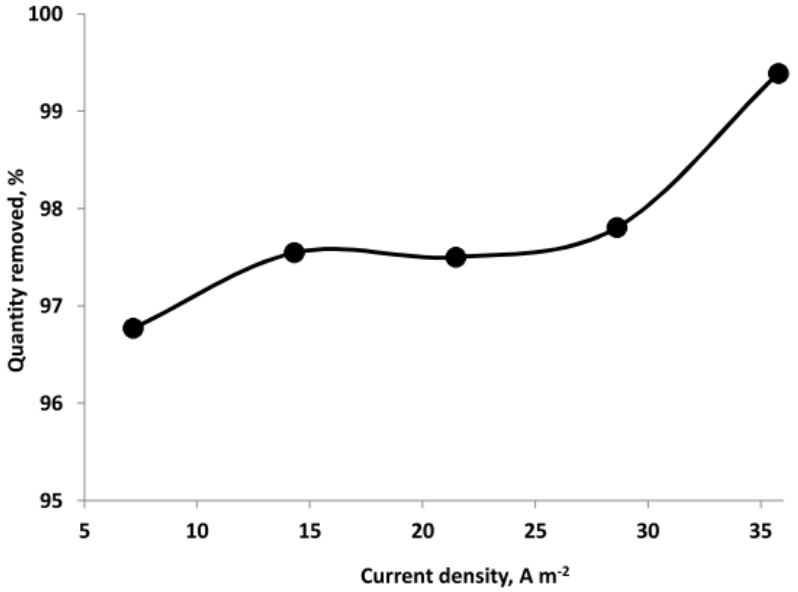

Figure 3. *Effect of current density on colour removal ([ARS] = 50 mg L^{-1}, T = 30 ^{o}C, pH 7.0 and [NaCl] = 2 g L^{-1}).*

Effect of pH on electrocoagulation process

pH is an important parameter influencing the performance of the EC process [34], it affects the chemistry of both the coagulants, dye molecules and that of electrochemical process in the solution. The effect pH on the removal of ARS was studied at initial pH varied between 3 and 11. The pH was adjusted with 0.1 M NaOH or 0.1 M HCl. The color removal percentages for dye solutions with various initial pH values were shown in Fig. 4.

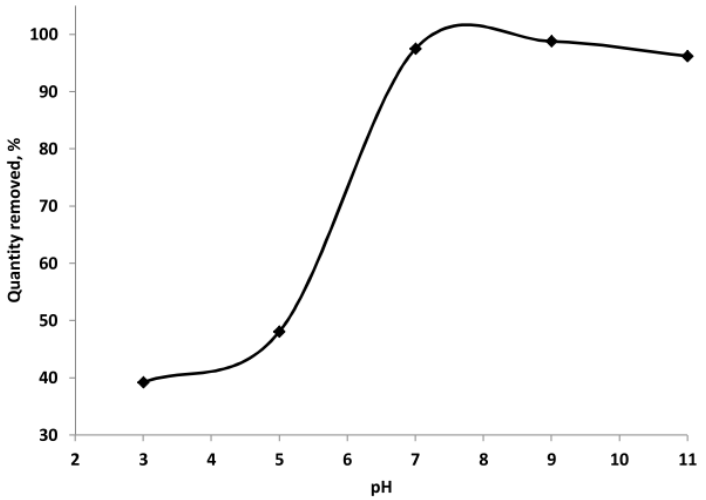

Figure 4. *Effect of initial pH on colour removal ([ARS] = 50 mg L^{-1}, T = 30 ^{o}C, [NaCl] = 2 g L^{-1}, j = 21.5 A m^{-2})*

The colour removal efficiency are optimum at the at pH range of 6.5 and 7.5 with about 97.5 % colour removal. The decrease in removal efficiency at more acidic and alkaline pH had been attributed to amphoteric behaviour of $Al(OH)_3$ which leads to soluble Al^{3+} cations (at acidic pH) and

formation of monomeric anions (at alkaline pH). These ions transform finally into solid $Al(OH)_3$ according to complex precipitation kinetics thereby affecting the removal efficiency [35,36].

Effect of electrolyte concentration

Solution conductivity influences the current efficiency, cell voltage and consumption of electrical energy in electrolytic cells. The use of NaCl to increase solution conductivity is also accompanied by the production of chloride ions that reduces the effects of other anions, such as bicarbonate and sulphate which may lead to the precipitation of Ca^{2+} leading to the high ohmic resistance of the electrochemical cell [17]. The tests of electrolyte concentration effects were performed in solutions containing a constant concentration of ARS 50 mg L^{-1}, at current density of 21.5 A m^{-2} and pH 7, while the concentrations of NaCl were varied between 1 to 5 g L^{-1}. Figure 5 shows that colour removal efficiency percentage increases from 86 to 97.6 % as the electrolyte concentration rises up to 2 g L^{-1}. A further increase in electrolyte concentrations beyond these values does not significantly affect the removal efficiency of the dye from the solution. The results also suggest that high colour removal percentage with low cell voltages and low energy consumption can be obtained at NaCl concentration of 2 g L^{-1}.

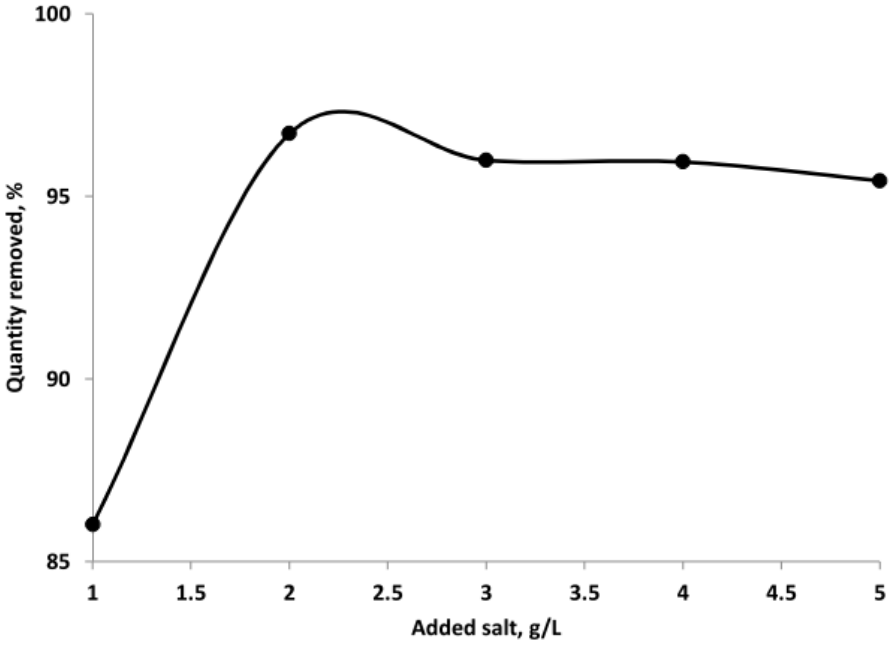

Figure. 5. *Effect of electrolyte concentrations on colour removal ([ARS] = 50 mg L^{-1}, T = 30 ^{o}C, pH = 7, j = 21.5 A m^{-2})*

Effect of initial dye concentrations

The effect of initial dye concentration on the electrocoagulation removal of ARS is shown in Figure 6 for dye concentrations increasing from 25 to 100 mg L^{-1} at constant temperature of 30 °C, current density 21.5 A m^{-2}, pH 7.0 and electrolyte concentration maintained with 2 g L^{-1} NaCl. The process showed rapid removal in the first 10 minutes for all the concentrations studied. The efficiency of the process increases from 138 to 604.8 mg g^{-1} as the initial concentration increases from 25 to 100 mg L^{-1}. As there is no significant difference in the amount coagulated after 20 minutes of the process, a steady-state approximation was assumed and a quasi-equilibrium situation was reached. The electrocoagulation curves were single, smooth, and continuous, leading to saturation. This is an indication of possible monolayer coverage on the surface of electrochemically generated coagulant [18,37].

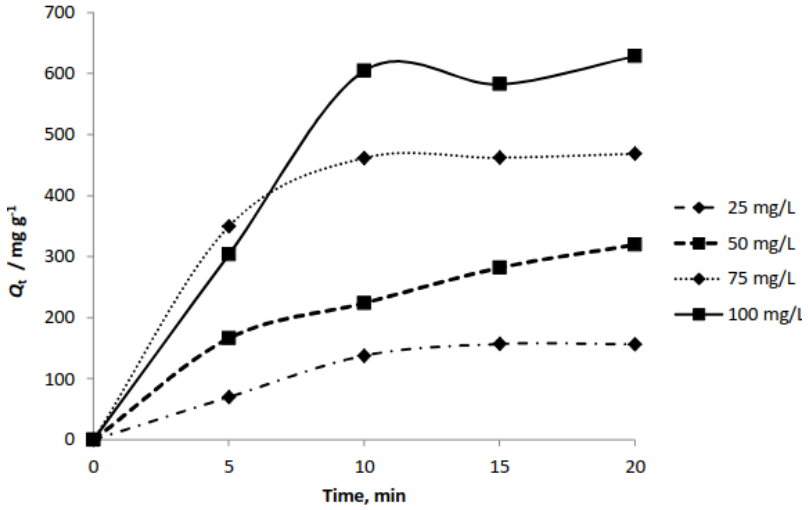

Figure 6. *Effect of initial concentration on the electrocoagulation removal of ARS (T = 30 °C, pH = 7, j = 21.5 A m^{-2} [NaCl] = 2 g L^{-1})*

Adsorption study

Adsorption isotherms

The adsorption data obtained at different initial dye concentrations were fitted into six different isotherm models. The equations representing these models and the parameters are summarized in Table 1, the details of which have been explained elsewhere [38].

Table 1. *Isotherm models used for the study of the EC removal of ARS*

Isotherm name	Isotherm model	Parameters
Langmuir	$Q_e = \frac{Q_{max} b C_e}{1 + b C_e}$	Q_{max} and b
Freudlinch	$Q_e = K_F C^{1/n}$	K_F and n,
Temkin	$Q_e = \frac{RT}{B_T} \ln(A_T C_e)$	A_T and B_T
Dubinin–Radushkevich	$Q_e = Q_s exp - \frac{\left(RT \ln\left(1 + \frac{1}{C_e}\right)\right)^2}{2E^2}$	Q_s and E
Redlich–Peterson	$Q_e = \frac{Q_o C_e}{(1 + K_R C_e^{\ g})}$	Q_o, K_R and g
Sip	$Q_e = \frac{Q_s (K_s C_e)^{\beta_s}}{(1 + (K_s C_e)^{\beta_s})}$	Q_s, K_s and β_s

The adsorption data fitted well with all the isotherms as shown in Figure 7, however, Dubinin--Radushkevich and Sip's isotherms have the highest R^2 (Table 2). The Q_m value of 785.31 mg g^{-1} obtained for the Langmuir isotherm model when compared with other isotherm Q values shows that the Dubinin–Radushkevich and Sip's isotherm values are lower than the Langmuir isotherm (Table 2). The $1/n$ value of > 1 obtained for Freudlinch isotherm is also indication that the adsorption is favorable.

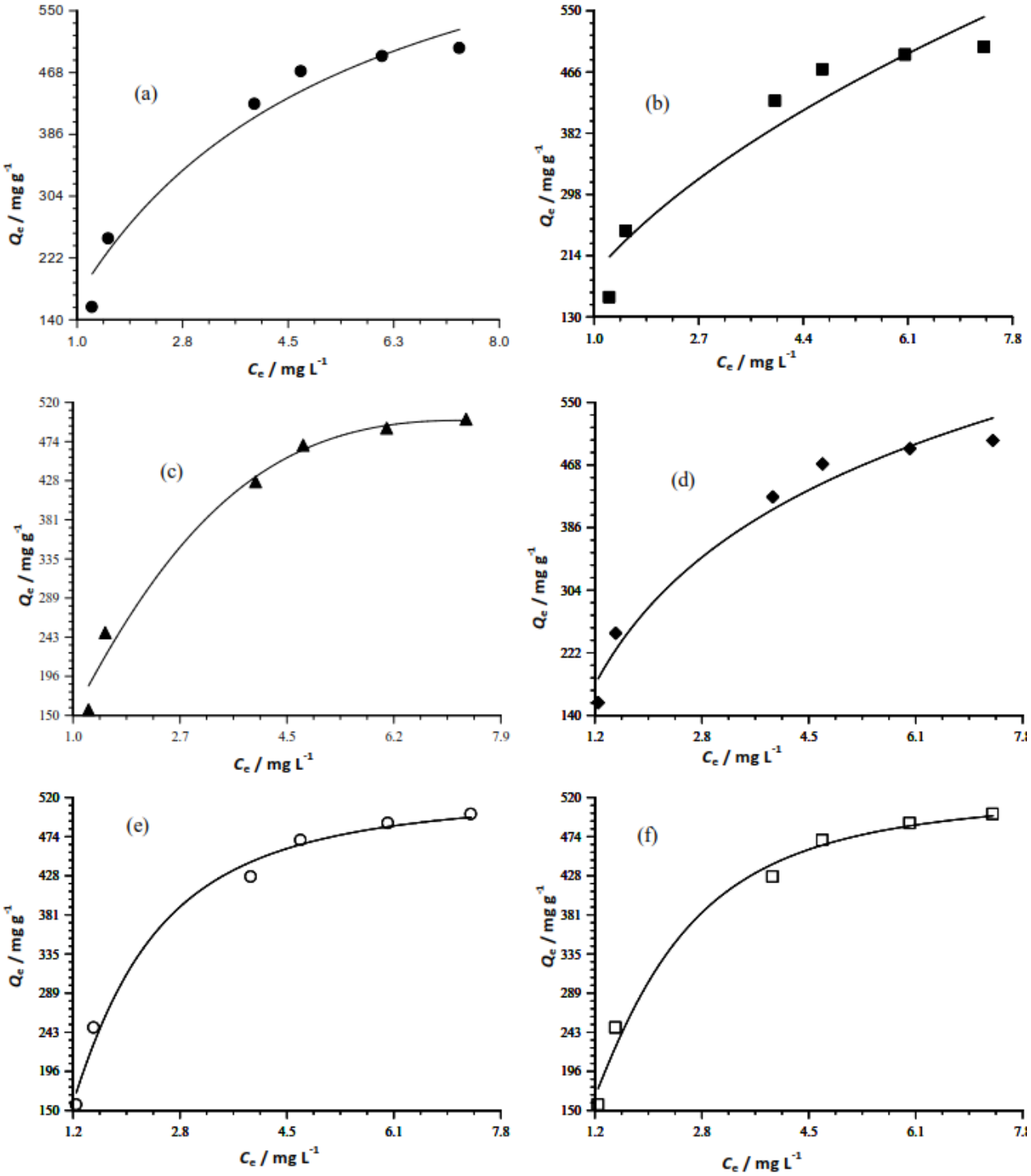

Figure 7. *Least square plots of the (a) Langmuir, (b) Freundlich, (c) Redlich–Peterson, (d) Temkin (e) Dubinin–Radushkevich and (f) Sips isotherms for electrocoagulation of Alizarin S dye at 30 °C.*

Table 2. *Isotherm parameters for electrocoagulation removal of Alizarin S*

Isotherms	Parameters	Values
Langmuir	Q_{max} / mg g^{-1}	785.31
	b / L mg^{-1}	0.27
	R_L	0.055
	R^2	0.996
Freudlinch	K_F / mg g^{-1} (mg L^{-1})$^{-1/n}$	188.85
	n	0.53
	R^2	0.992
Tempkin	A_T / L g^{-1}	13.06
	B_T / J mol^{-1} g mg^{-1}	2.12
	R^2	0.997
Dubinin–Radushkevich	Q_s / mg g^{-1}	653.10
	E / kJ mol^{-1}	5.65x10^{-7}
	R^2	0.941
Redlich–Peterson	Q_0 / mg g^{-1}	4372.23
	K_R / (mg^{-1} g)$^{1/g}$	0.036
	g	1.80
	R^2	0.998
Sips	Q_s / mg g^{-1}	524.63
	K_s / (mg^{-1} L)$^{1/\beta_s}$	0.57
	β_s	2.05
	R^2	0.999

Electrocoagulation kinetics

The plots of four different kinetic models used to explain the adsorption data are shown in Figure 8 (a - d). The equations for these models are shown in Table 3, details of which have explained elsewhere [38]. As shown in the figure, pseudo-first-order kinetic models fitted well with experimental data when compared with other models the R^2 value of the model also confirmed this (Table 4). The rate constant from all the models increases with initial dye concentration up to 75 mg L^{-1} before decreasing at 100 mg L^{-1}. This shows that at higher initial concentration the electrostatic interaction decreases at the site, thereby lowering the adsorption rate. The behaviour of Elovich constant shows that the process of adsorption is more than one mechanism.

Table 3: Kinetic models for the EC process

Isotherm name	Isotherm model	Parameters
Pseudo First Order	$Q_t = Q_e(1-e^{(-k_1 t)})$	Q_e and k_1
Pseudo Secon Order	$Q_t = \frac{Q_e^2 k_2 t}{(1+Q_e k_2 t)}$	Q_e and k_2
Elovich	$Q_t = \frac{1}{\beta}\ln(\alpha\beta t)$	α and β
Avramin	$Q_t = Q_e(1-e^{-k_{av}t^{n_{av}}})$	k_{av}, and n_{av}
Intraparticulate model	$Q_t = K_{id}t^{0.5} + C_i$	K_{id} and C_i

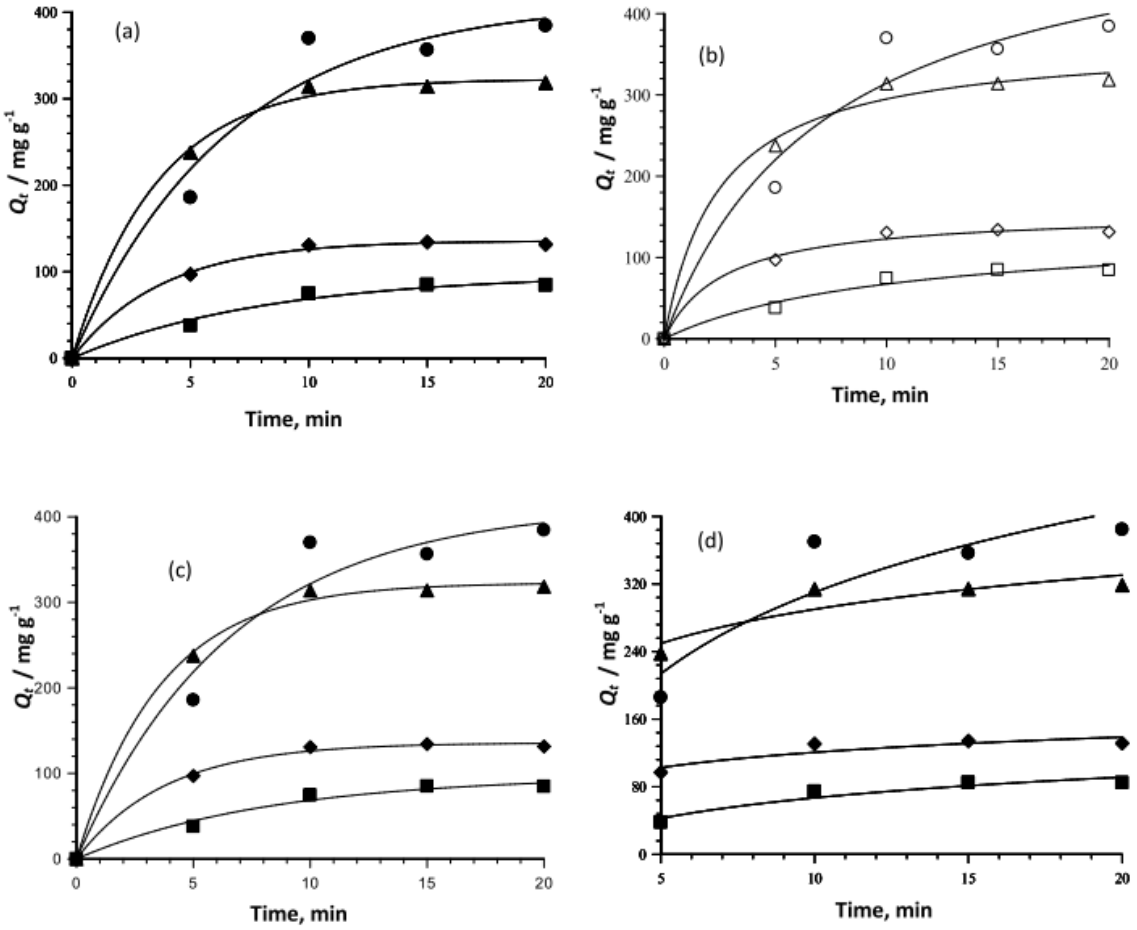

Figure 8. *Least square plots of (a) pseudo-first-order, (b) pseudo-second-order, (c) Avramin and (d) Elovich kinetic models for Alizarin S dye electrocoagulation at 30 ^{o}C.*

Table 4. *Comparison of kinetic model constant values for Alizarin Red S removal by electrocoagulation*

	$C_{0\,/}$ mg L^{-1}	25.00	50.00	75.00	100.00
	$Q_{e\,exp}$ / mg g^{-1}	74.52	130.75	313.80	369.92
First order	$Q_{e\,cal}$ / mg g^{-1}	97.30	135.75	322.81	413.23
	k_1 / min^{-1}	0.12	0.26	0.28	0.15
	R^2	0.995	0.999	0.997	0.992
	SSE, %	6.11	0.76	0.57	2.34
Second order	$Q_{e\,cal}$ / mg g^{-1}	136.04	155.88	367.39	548.90
	k_2 10^{-3} / g mg^{-1} min^{-1}	0.7204	2.3817	1.1079	0.2444
	R^2	0.993	0.998	0.998	0.989
	SSE, %	16.51	3.84	3.42	9.68
Avramin	$Q_{e\,cal}$ / mg g^{-1}	97.30	135.75	322.81	413.23
	k_{av} / min^{-1}	0.35	0.51	0.53	0.39
	n_{av}	0.35	0.51	0.53	0.39
	SSE, %	6.11	0.76	0.57	2.34
	R^2	0.995	0.999	0.999	0.992
Elovich	β / g mg^{-1}	0.03	0.04	0.02	0.01
	α / mg (g min)$^{-1}$	23.52	267.45	840.16	129.21
	R^2	0.993	0.997	0.998	0.989
	SSE, %	13.69	20.91	33.55	13.01

Adsorption mechanism

The mechanism of adsorption was investigated by subjecting the data to intra-particulate diffusion model. The plots are shown in Figure 9. The plots are not linear over the whole time range but rather they exhibit multi-linearity revealing the existence of two successive adsorption steps. The first stage is faster than the second, and it is attributed to the external surface adsorption referred to as the boundary layer diffusion. Thereafter, the second linear part is attributed to the intra-particle diffusion stage; this stage is the rate controlling step. Table 5 shows the intra-particle model constants for the electrocoagulation removal of ARS dye. The K_{di} values were found to increase from first stage of adsorption toward the second stage. The increase in dye concentration results in an increase in the driving force thereby increasing the dye diffusion rate.

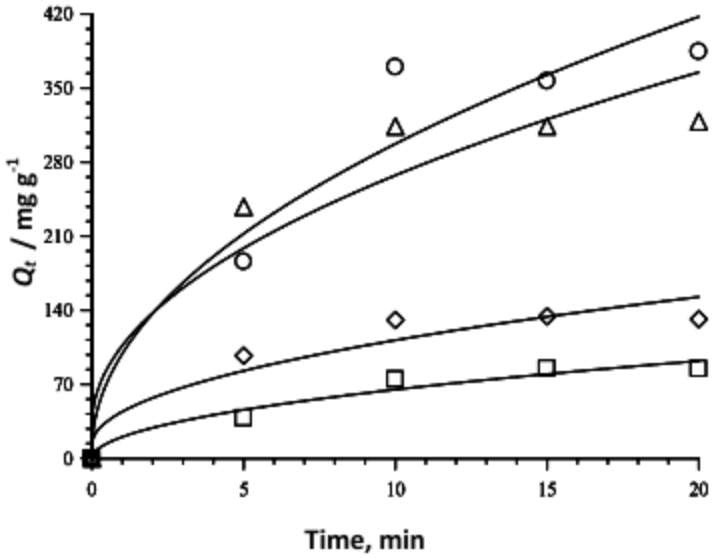

Figure 9. *Intraparticulate diffusion model plots for Alizarin S dye electrocoagulation at 30 °C.*

Table 5. *Intra-particle diffusion model for the electrocoagulation removal of Alizarin S*

C_o / mg L^{-1}	25	50	75	100
K_{d1} / mg g^{-1} min$^{-0.5}$	22.34	41.72	100.53	110.72
K_{d2} / mg g^{-1} min$^{-0.5}$	7.92	0.68	3.39	10.23
C_1	-2.73	0.85	2.91	-14.00
C_2	50.97	129.52	302.38	331.09
R_1^2	0.980	0.999	0.999	0.979
R_2^2	0.999	0.999	0.999	0.999

Thermodynamic parameters

Figure 10 shows that the rate constants vary with temperature according to Equation 9. The activation energy (3.55 kJ mol^{-1}) was obtained from the slope of the fitted equation. The free energy change, Δ*G* is obtained from Equations 10 and 11 according to the van't Hoff linear plots of ln K_d versus 1/*T* plot in Figure 10 (a and b). The thermodynamic parameters are presented in Table 6. It was found that the negative value of Δ*G* indicates the spontaneous nature of adsorption. Positive value of enthalpy change indicates that the adsorption process is endothermic in nature, and the negative value of change in internal energy (Δ*G*) shows the spontaneous adsorption of ARS on the coagulant. Positive values of entropy change show the increased randomness of the solution interface during the adsorption process (Table 6).

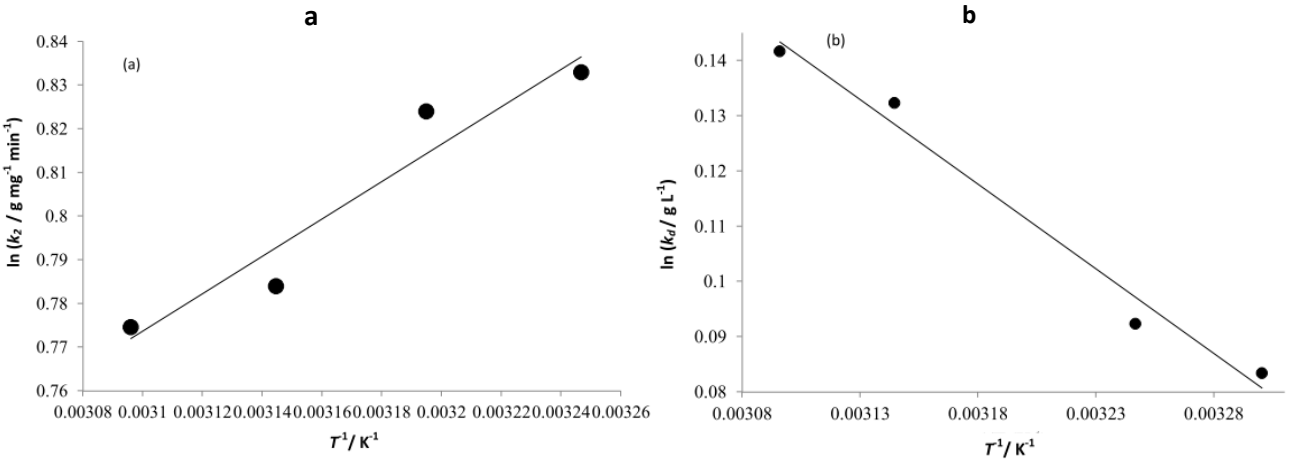

Figure 10. *Thermodynamic plot (a) ln* k_2 *and 1/**T** and (b) ln* K_d *and 1/*T *for the removal of Alizarin S dye by electrocoagulation.*

Table 6. *Thermodynamic parameters for the removal of Alizarin S*

T / K	*K*	Δ*G* / kJ mol^{-1}	E_a / kJ mol^{-1}	Δ*S* / bJ mol^{-1}	Δ*H* / kJ mol^{-1}	R^2
303	1.0870	-5.301	3.55	9.083	2.549	0.981
308	1.0967	-5.346				
318	1.1415	-5.437				
323	1.1522	-5.483				

FT-IR Studies of the dye solution before and after electrocoagulation

Figure 11 presents the FT-IR spectrum of the dye solution before and after the process. Before the electrocoagulation the spectrum shows several peaks; sharp and strong peak at 3440.8 cm^{-1} could be assigned to –OH stretching on the dye molecule while, that at 2821 cm^{-1} is due to –CH–. Peaks at 1593 and 1350 cm^{-1} are due to the aromatic C=C stretching. After electrocoagulation, the extra structure noted such as that at 3840 cm^{-1} may be assigned to the (O–H) stretching vibration in the Al(OH)$_3$ structures.

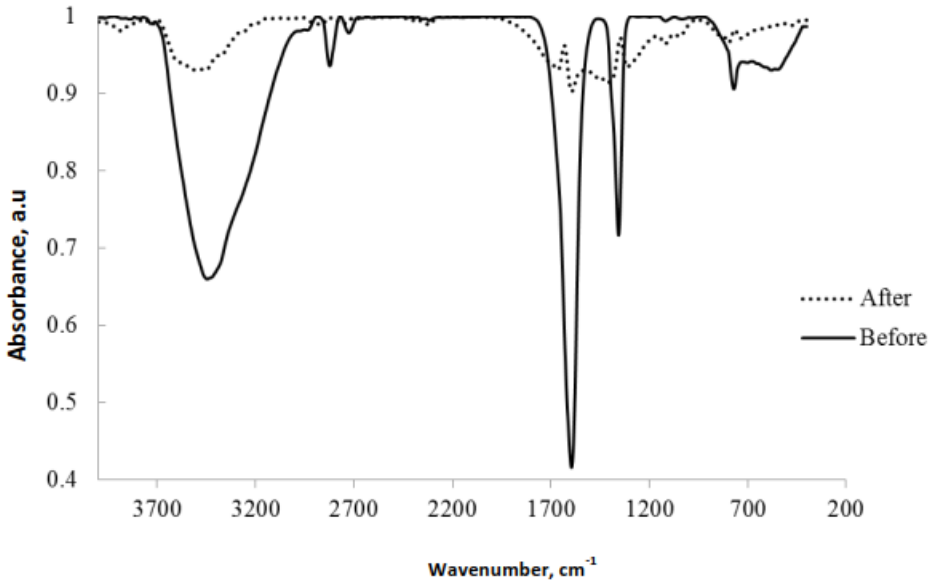

Figure 12. *FTIR of the solution of Alizarin Red S dye before and after removal*

Conclusions

This study revealed the feasibility of the use of electrocoagulation techniques for removing Alizarin Red S from its aqueous solution in a process. The process depends on numerous factors such as: current density, solution pH, temperature, initial dye concentration and contact time. The percentage removal of the dye increased with pH up to pH 7, also contact time and current density increase influence the removal positively. Equilibrium data fitted very well in the Langmuir isotherm equation, confirming the monolayer adsorption capacity of 785.31 mg g^{-1} at 303 K. The kinetics of the process is best explained using a pseudo first order kinetics model, with higher R^2 (Table 4). Intra-particle diffusion was not the sole rate controlling factor. The thermodynamics parameters obtained indicates that the process is spontaneous endothermic nature of the process. Therefore, the present findings suggested a better performance of electrocoagulation with Al electrode as an inexpensive method for the removal of ARS aqueous solutions.

Acknowledgements*: The financial support in the form of grants from CSIR, for twelve months TWAS-CSIR Postdoctoral Fellowship, FR number: 3240275035, awarded to Abideen Idowu Adeogun that enables this work to be carried out. Also he is thankful to the authority of the Federal University of Agriculture, Abeokuta, Nigeria for granting the study leave to honour the fellowship.*

References

[1] G. Crini, *Bioresources Technology* **97** (2006) 1061-1085.
[2] S. Rajgopalan, *Pollution Management in Industries* Trivedy RK (Eds.) Environmental Publications, Karad., India (1995) p. 44.
[3] T. Routh, *Journal of Environmental Protection* **20(2)** (1998) 115-123.
[4] D.W.Kolpin, E.T. Furlong, M.T. Meyer, E.M. Thurman S.D. Zaugg, L.B. Barber, H.T. Buxton, *Environmental Science and Technology* **36(6)** (1999–2000) 1202-1211.
[5] M. Ali, T.R. Sreekrishnan, *Advance in Environmental Research* **5** (2001) 175-196.
[6] Q.Y. Sun, L.Z. Yang, *Water Research* **37** (2003) 1535-1544.
[7] R.A. Shawabkeh, M.F. Tutunji, *Applied Clay Science* **24(1–2)** (2003) 111-120.
[8] G.H. Lin, D.J. Brusick, *Journal of Applied Toxicology* **12(4)** (1992) 267-274.
[9] P. Zucca, C. Vinci, F. Sollai, A. Rescigno, E. Sanjust, *Journal of Molecular Catalysis A: Chemical* **288** (2008) 97-102.
[10] P.A. Carneiro, M.E. Osugi, C.S. Fugivar, N. Boralle, M. Furlan, M.V. Zanoni, *Chemosphere* **59(3)** (2005) 431-439.
[11] M. Panizza, P.A. Michaud, G. Cerisola, C. Comninellis, *Electrochemistry Communications* **3** (2001) 336-339.
[12] Z.X. Wang, X.C. Xu, Z. Gong, F.Y. Yang, *Journal of Hazardous Materials* **78(1)** (2012) 235-236.
[13] A. Aleboyeh, N. Daneshvar, M. B. Kasiri, *Chemical Engineering Process* **47** (2008) 827-832.
[14] F. Ghanbari, M. Moradi, A. Eslami, M.M. Emamjomeh, *Environmental Process* **1** (2014) 447-457.
[15] M.O. Nkiko, A.I. Adeogun, N.A.A. Babarinde, O. J. Sharaibi, *Journal of Water Reuse and Desalination* **3(3)** (2013) 239-248.
[16] B. Merzouk, M. Yakoubi, I. Zongo, J.P. Leclerc, G. Paternotte, S. Pontvianne, F. Lapicque *Desalination* **275(1–3)** (2011) 181-186.
[17] J. Zolgharnein, M. Bagtash and N. Asanjarani, *Journal of Environmental and Chemical Engineering* **2** (2014) 988-1000.
[18] T. Moriguchi, K. Yano, S. Nakagawa, F. Kaji, *Journal of Colloidal Interface Science* **260** (2003) 19-25.

[19] M. Ghaedi, A. Hassanzadeh, S.N. Kokhdan, *Journal of Chemical Engineering and Data* **56** (2011) 2511-2520.
[20] C. Saez, M. Panizza, M.A. Rodrigo, G. Cerisola, *Journal of Chemical Technology and Biotechnology* **82(6)** (2007) 575 - 581.
[21] M. Panizza, M.A. Oturan, *Electrochimica Acta* **56** (2011) 7084 – 7087.
[22] F. Yi, S. Chen, C. Yuan *Journal of Hazardous Materials* **B157** (2008) 78-87.
[23] M. Panizzan, G. Cerisola, *Water Research* **43** (2009) 339.
[24] N. Daneshvar, A. Oladegaragoze, N. Djafarzadeh, *Journal of Hazardous Materials* **B129** (2006) 116-122.
[25] I. Langmuir, *Journal of* American *Chemical Society* **40** (1918) 1361-1403.
[26] H.M.F. Freundlich, Journal of Physical Chemistry **57** (1906) 385-471.
[27] M.I. Tempkin, V. Pyzhev, *Acta Physica Chimca USSR* **12** (1940) 327–356.
[28] M.M. Dubinina, L.V. Radushkevich, *Izvestiya Akademii nauk, fizicheskoy khimii sektsii USSR* **55** (1947) 331-333.
[29] R. Sips, *Journal of Chemical Physics* **16** (1948) 490-495.
[30] O. Redlich, D.L. Peterson, *Journal of Physical Chemistry* **63** (1959) 1024-1026.
[31] T.S Aniruldhan, P.G. Radhakrishnan, *Journal of Chemical Thermodynamics* **40** (2008) 702-709.
[32] N. Daneshvar, A. Oladegaragoze, N. Djafarzadeh *Journal of Hazardous Materials* **B129** (2006) 116-122.
[33] N. Daneshvar, D. Salari, A. R. Khataee, *Journal of Photochemistry and Photobiology* **A 157** (2003) 111-116.
[34] M.Y.A. Mollah, P. Morkovsky, J.A.G. Gomes, M. Kesmez, J. Parga, D.L. Cocke, *Journal of Hazardous Materials* **B 114** (2004) 199-210.
[35] M. Bayramoglu, M. Kobya, O. Can, T.M. Sozbir, *Separation Purification Technology* **37** (2004) 117-125.
[36] M. Kobya, E. Demirbas, A. Dedeli, M.T. Sensoy, *Journal Hazardous Material* **173** (2010) 326-334.
[37] P. Saha, S.K. Sanyal, *Desalination,* **59** (2010) 131-139.
[38] A.I. Adeogun, B.R. Balakrishnan*, Applied Nanoscience* (2015) Doi: 10.1007/s13204-015-0484-9.